Fresnel-Focusing and Bessel-Beam Integrated Optical Phased Arrays for Optical Trapping Applications

by

Jelena Notaros

B.S., University of Colorado Boulder (2015)

Submitted to the
Department of Electrical Engineering and Computer Science
in partial fulfillment of the requirements for the degree of

Master of Science in Electrical Engineering and Computer Science

at the

MASSACHUSETTS INSTITUTE OF TECHNOLOGY

June 2017

Author ..... Signature redacted ....
Department of Electrical Engineering and Computer Science
May 12, 2017

Certified by ..... Signature redacted
Michael R. Watts
Associate Professor of Electrical Engineering
Thesis Supervisor

Accepted by ..... Signature redacted
Leslie A. Kolodziejski
Professor of Electrical Engineering
Chair of the Department Committee on Graduate Students

Fresnel-Focusing and Bessel-Beam Integrated Optical Phased Arrays for Optical Trapping Applications

by

Jelena Notaros

Submitted to the Department of Electrical Engineering and Computer Science
on May 12, 2017, in partial fulfillment of the
requirements for the degree of
Master of Science in Electrical Engineering and Computer Science

Abstract

Optical trapping and tweezing – the manipulation of particles using optical forces – enables direct interaction with biological samples and non-invasive monitoring of their properties. As such, optical trapping has become a common tool in biology with applications ranging from better understanding of DNA mechanics to non-invasive manipulation of red blood cells *in vivo*. While optical trapping using bulk optics is a well established technique, recent work has turned towards chip-based optical trapping using integrated devices. However, many of these integrated systems are fundamentally limited to passive demonstrations within microns of the chip surface.

Integrated optical phased arrays, which manipulate and dynamically steer light, provide one possible approach to scaling and arbitrary tweezing of optical traps. However, current on-chip optical phased array demonstrations have focused on systems which form and steer beams or project arbitrary radiation patterns in the far field.

In this thesis, Fresnel-lens-inspired focusing integrated optical phased arrays are demonstrated for the first time and proposed as a method for chip-based optical trapping. These systems focus radiated light to tightly-confined spots in the near field above the chip to enable applications in wide-angle trapping at millimeter scales. Furthermore, integrated optical phased arrays are proposed and demonstrated for the first time as a method for generating quasi-Bessel beams in a fully-integrated, compact-form-factor system. Through generation of quasi-Bessel beams with elongated properties, these devices have potential for applications in multi-particle, multi-plane optical trapping. To enable these phased array systems, a suite of integrated nanophotonic architectures and devices for waveguiding, coupling, routing, phase control, and radiation are developed, simulated, fabricated, and tested and a CMOS-compatible foundry platform is leveraged for natural scaling to active demonstrations.

Thesis Supervisor: Michael R. Watts
Title: Associate Professor of Electrical Engineering

To the pioneering giants of electromagnetics and photonics

for providing the foundation of this thesis.

To my current and past advisors and professors

for helping me to nearly understand and fully love this field.

To my group members throughout the years

for all the collaborations and friendships.

To Branislav, Olivera, Milica, and Tesh

for everything else.

Contents

List of Figures

List of Tables

Chapter 1

Introduction

1.1 Introduction to Optical Trapping

Optical traps and tweezers enable trapping and manipulation of particles through non-contact forces caused by optical intensity gradients and photon momentum transfer [1, 2]. Due to these properties, optical trapping has become a common tool in biology since it enables direct interaction with biological samples and non-invasive monitoring of their properties [2, 3]. For example, this technique has been used to better understand DNA mechanics [4], for non-invasive manipulation of red blood cells *in vivo* [5], to study kinetochore-microtubule attachments [6], for real-time Raman spectroscopy of living cells [3], and for tracking of cell growth [7]. Moreover, optical trapping has been used as a tool for microfabrication using nanowires and microrods [8, 9] and for quantum computing using trapped ions [10, 11].

While optical trapping using bulk optics is a well established technique, recent work has turned towards chip-based optical trapping using integrated devices such as photonic crystal nanocavities [12–16], plasmonic nanoantennas [17–20], and microring resonators [21, 22], as shown in Fig. 1.1. However, these systems have been limited to trapping either directly on or within microns of the chip surface. Moreover, many of these devices have been fundamentally limited to passive trapping demonstrations which prevent any optically-driven manipulations. Dynamic and wide-angle integrated tweezing at millimeter scales above the chip – especially advantageous for

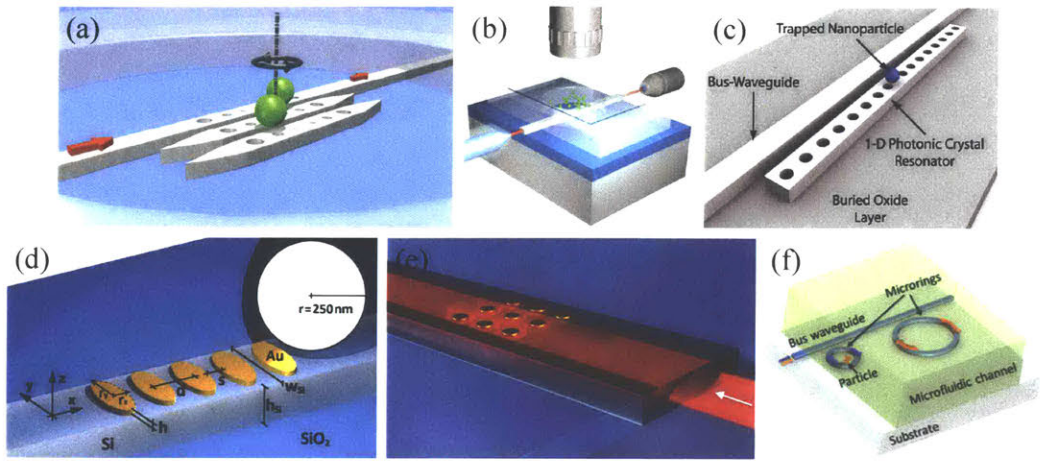

Figure 1.1: Overview of select chip-based integrated optical trapping demonstrations using (a–c) photonic crystal nanocavities (figures from [13–15]), (d–e) plasmonic nanoantennas (figures from [17, 20]), and (f) microring resonators (figure from [21]).

in vivo applications [5] – has not been demonstrated.

1.2 Introduction to Optical Phased Arrays

Integrated optical phased arrays, which manipulate and dynamically steer light with large aperture sizes [23] and the potential for 200 MHz rates [24], provide one possible approach to scaling and arbitrary tweezing of optical traps.

Historically, radio-frequency (RF) phased antenna arrays have enabled the development and advancement of numerous applications such as radio transmitters, radar, television broadcasting, and radio astronomy. However, due to the relatively long wavelengths of RF frequencies, large-scale implementation of these arrays – necessary for generation of ultra-high resolution and arbitrary radiation patterns – is cumbersome and expensive. As a solution, optical phased arrays, operating at much shorter optical wavelengths and fabricated in integrated nanophotonic platforms, open up possibilities for large-scale applications in a variety of areas including three-dimensional holography, biomedical sciences, communications, and light detection and ranging (LIDAR) [25].

Current on-chip optical phased array demonstrations have focused on systems

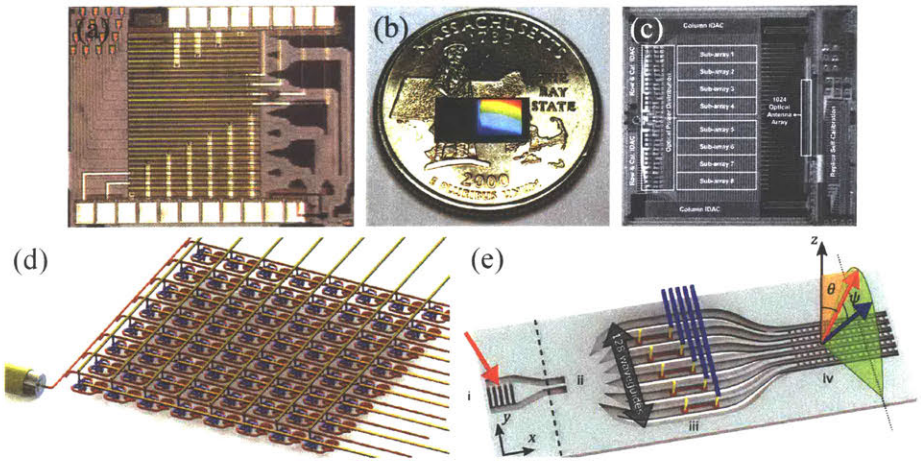

Figure 1.2: Overview of select integrated optical phased array demonstrations (figures from [23–27]).

which form and steer beams or project arbitrary radiation patterns in the far field, as shown in Fig. 1.2 [23–30]. However, since optical forces are formed due to intensity gradients, optical trapping requires a system with a tightly-focused spot in the near field of the array. (Near-field optical phased array manipulation has only recently been theoretically explored for holography applications [31].)

1.3 Thesis Overview

In this thesis, Fresnel-lens-inspired focusing integrated optical phased arrays are demonstrated for the first time and proposed as a method for chip-based optical trapping. These systems focus radiated light to tightly-confined spots in the near field above the chip to enable applications in wide-angle trapping at millimeter scales. Furthermore, integrated optical phased arrays are proposed and demonstrated for the first time as a method for generating quasi-Bessel beams in a fully-integrated, compact-form-factor system. Through generation of quasi-Bessel beams with elongated central beams, these devices have potential for applications in multi-particle, multi-plane optical trapping. This work has led to three publications upon which this thesis is based [32–34].

Foremost, in Ch. 2, the phase distributions necessary for generating focusing

beams are derived, and discussion and simulations detailing the effect of the array aperture and focal height on the full-width half-maximum (FWHM) of the focused spot are provided. Additionally, the effect of conventional linear steering on the focal height is shown and a modified non-linear steering phase is derived.

In Ch. 3, Bessel and Bessel-Gauss beam generation is discussed and the derived near-field phased array theory is extended to develop the phase and amplitude distributions necessary for generating phased-array-based Bessel-Gauss beams analogous to bulk-optics Bessel implementations. Discussion and simulations detailing the effect of the array aperture and element parameters on the central-beam FWHM and Bessel length of the generated beam are presented.

Next, two integrated optical phased array architectures are proposed for experimentally demonstrating near-field focusing and quasi-Bessel-beam-generating optical phased arrays. First, in Ch. 4, a one-dimensional (1D) splitter-tree-based phased array architecture [23,35] is modified to passively encode arbitrary phase and amplitude distributions to the elements of the array – necessary for focusing-beam and Bessel-Gauss-beam generation – in both a silicon and a silicon-nitride platform. An overview of the architecture and foundry fabrication processes are presented and the various integrated nanophotonic components of the systems are developed, numerically simulated, and experimentally demonstrated. Second, in Ch. 5, a two-dimensional (2D) pixel-based architecture [25] is utilized to show a second type of passive focusing and Bessel-Gauss-generating phased array with capabilities for active electronic focusing in two dimensions. The architecture and corresponding nanophotonic system components are developed for two foundry processes with numerical device characterization data presented.

In Ch. 6, the developed theory and system architectures are utilized to experimentally demonstrate a variety of focusing integrated optical phased arrays with varying aperture sizes and focal heights. First, the silicon-nitride splitter-tree-based architecture is utilized to show a 1D-focusing integrated phased array with capabilities for high-power operation. The 128-antenna array focuses the radiated light in one-dimension to a line with a $\sim$13 μm FWHM at a 5 mm focal height. Second,

the silicon splitter-tree-based architecture is implemented to demonstrate both 1D- and 2D-focusing integrated phased arrays with a variety of focal heights, including a 512-antenna array with a $\sim$7 μm spot at a 5 mm focal height. Additionally, experimental data showing wavelength steering of these arrays in the antenna dimension is demonstrated and discussion on extension of the splitter-tree-based architecture to electronic control in the array dimension is presented. Third, the two-dimensional pixel-based architecture is utilized to enable a variety of 2D-focusing phased arrays with capabilities for active electronic focusing in two dimensions, including a 1024-antenna array with a $\sim$21 μm spot at a 5 mm focal height and a 10,000-antenna array with a $\sim$21 μm spot at a 10 mm focal height.

In Ch 7, both of the developed architectures are used to experimentally demonstrate on-chip quasi-Bessel-beam generation. First, the silicon-nitride splitter-tree-architecture is implemented to generate a quasi-one-dimensional Bessel-Gauss beam with a $\sim$14 mm Bessel length and $\sim$30μm central-beam FWHM. Second, the pixel-based architecture is used to demonstrate Bessel-Gauss-beam generation in two dimensions with a $\sim$30μm central-beam FWHM and discussion is presented on extension of the system to generation of a radial-symmetric Bessel-Gauss beam.

Chapter 2

Focusing Phased Array Theory

In this chapter, focusing phased array theory is derived and discussed. First, the field generated by a standard, non-focusing array is calculated in the near-field of the array as a comparison. The element phase distributions necessary for generating focusing beams in the near field are then derived and the resulting fields are compared. Next, the effects of the array aperture and focal height on the full-width half-maximum (FWHM) of the focused spot are simulated and compared to bulk optics theory. Finally, the effect of the conventional linear steering phase on focusing phased arrays is shown and a modified non-linear steering phase is derived.

2.1 Element Phase Derivation and Focusing Phased Array Simulations

In general, a phased array is a system comprised of an array of antennas that are fed with controlled phases and amplitudes, as shown in Fig. 2.1a, to generate arbitrary radiation patterns [36]. If the antennas are spaced with a uniform pitch, d, and fed with a uniform amplitude and a linear phase distribution, the array creates a steerable, diffracting beam in the far field of the array. The near-field electric-field profile generated by this phased array can be approximated by summing the electric-

field components of each element in the array:

$$E(x,y,z) = \sum_{n=1}^{N} E_n(x,y,z) \approx \sum_{n=1}^{N} e^{-i(2\pi r_n/\lambda + \Phi_n)} \tag{2.1}$$

where N is the total number of antennas in the array, Φ_n is the phase applied to the nth antenna, r_n is the distance from the nth antenna to the point under consideration at coordinate (x, y, z), and λ is the propagation wavelength. Using this method, a standard array with $N = 512$, $d = 2\,\mu\text{m}$, and $\lambda = 1550\,\text{nm}$ is simulated; the generated intensity profile is shown in Fig. 2.2a.

In contrast, if a "lens-like" hyperbola element phase distribution is applied, the array will focus light into a tightly-confined spot in the near field above the array. This element phase is derived by calculating the relative delay necessary such that constructive interference of the wavefronts occurs at the focal point. First, the distance from each antenna to the focal point is calculated as:

$$L_n = \sqrt{f_z^2 + d^2\left(N/2 + 1/2 - n\right)^2} \tag{2.2}$$

where f_z is the desired focal height as shown in Fig. 2.1a. To enforce the focusing condition, the phase applied to each antenna should compensate for the differences

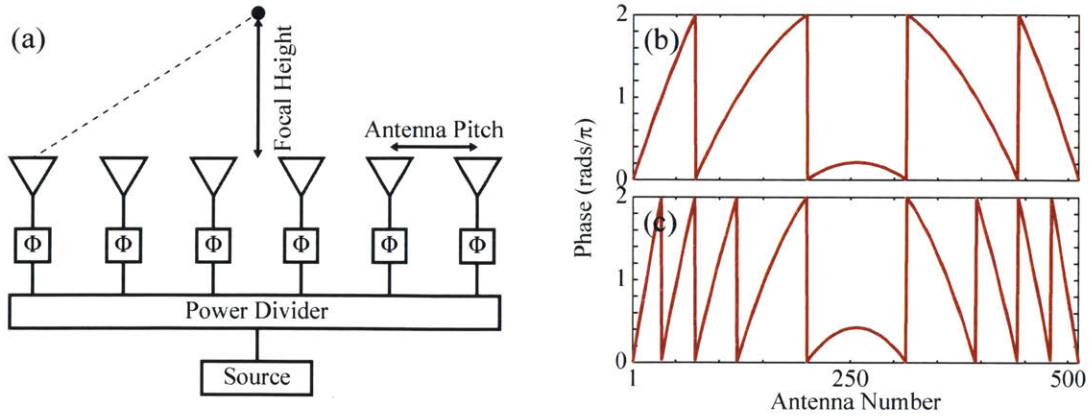

Figure 2.1: (a) Schematic of a generalized focusing phased array showing the antenna pitch and focal height. Element phase distributions for a focusing phased array with (b) $f_z = 40\,\text{mm}$ and (c) $f_z = 20\,\text{mm}$ focal height assuming 512 antennas, 2 μm antenna pitch, and 1550 nm wavelength.

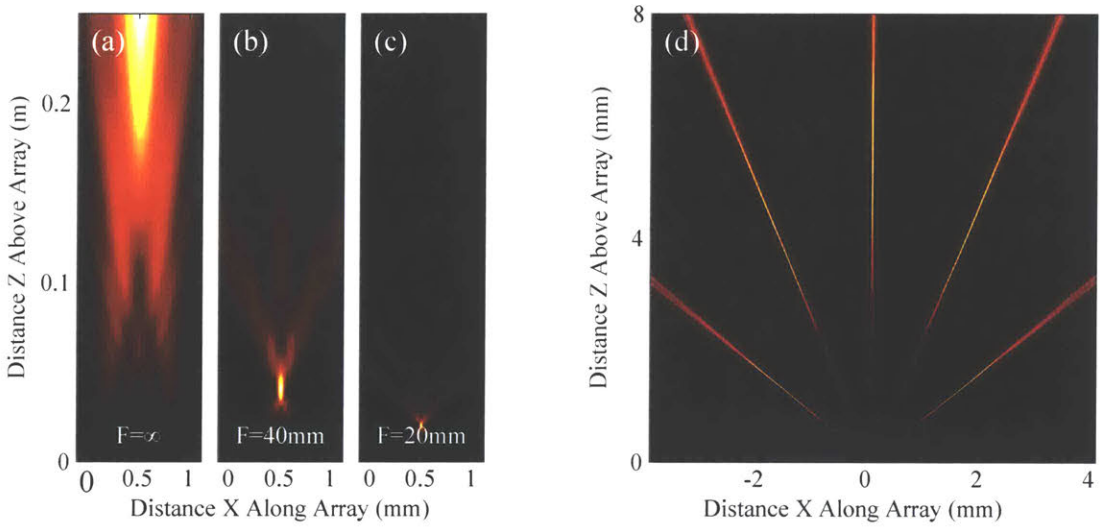

Figure 2.2: Simulated array-factor intensity above the array for a (a) non-focusing, (b) $f_z = 40\,\text{mm}$ focal height, and (c) $f_z = 20\,\text{mm}$ focal height phased array with 512 antennas, $2\,\mu\text{m}$ antenna pitch, and 1550 nm wavelength. Simulated array-factor intensity above the array showing higher-order grating lobes for a $f_z = 5\,\text{mm}$ focal height phased array with 64 antennas, $4\,\mu\text{m}$ antenna pitch, and 1550 nm wavelength.

in the corresponding optical path lengths such that the wavefronts at the focal point constructively interfere. This gives the desired feeding phase distribution

$$\Phi_n = \frac{2\pi}{\lambda}\left(L_1 - L_n\right). \tag{2.3}$$

Similarly to a Fresnel lens, this phase can be encoded modulo 2π as shown in Fig. 2.1b–c.

Figures 2.2b–c show the simulated intensity profiles generated by two focusing phased arrays with $N = 512$, $d = 2\,\mu\text{m}$, $\lambda = 1550\,\text{nm}$, and varying focal heights. As shown, by applying the derived element phase profiles, the arrays focus light to tightly-confined and highly-enhanced spots. Additionally, due to discretization of continuous theory onto arrays with $d > \lambda/2$, higher-order grating lobes are generated by the arrays at larger angles as shown in Fig. 2.2d. These higher-order grating lobes also exhibit focusing properties although they do not focus at the design focal height. Since these additional beams reduce the power radiated into the main focal spot and limit the possible steering range without aliasing of the main beam [36],

tighter antenna pitches are desired.

2.2 Parameters and Limits of Focusing Phased Arrays

For appreciable focusing, the desired focal height of a focusing array should be limited to the Fresnel region (i.e. the near field) of the phased array, $r_{near} \approx A^2/\lambda$ where $A = Nd$ is the aperture size, as given by antenna theory [36]. Consequently, by increasing the array aperture size, the possible focal height of the array quadratically increases.

Additionally, for potential applications which require highly-enhanced and tightly-focused spots, a valuable figure of merit of a focusing array is the power FWHM of the resulting spot at the desired focal height. For example, for a 512-antenna array with a 2 μm antenna pitch at a 1550 nm wavelength as simulated in Figs. 2.2b–c, the FWHM is found to be 53.5 μm and 26.6 μm for focal heights of 40 mm and 20 mm, respectively.

Similar to bulk lenses, the FWHM depends on the aperture size of the array and the focal height. As shown in Fig. 2.3a, as the array aperture size increases, the

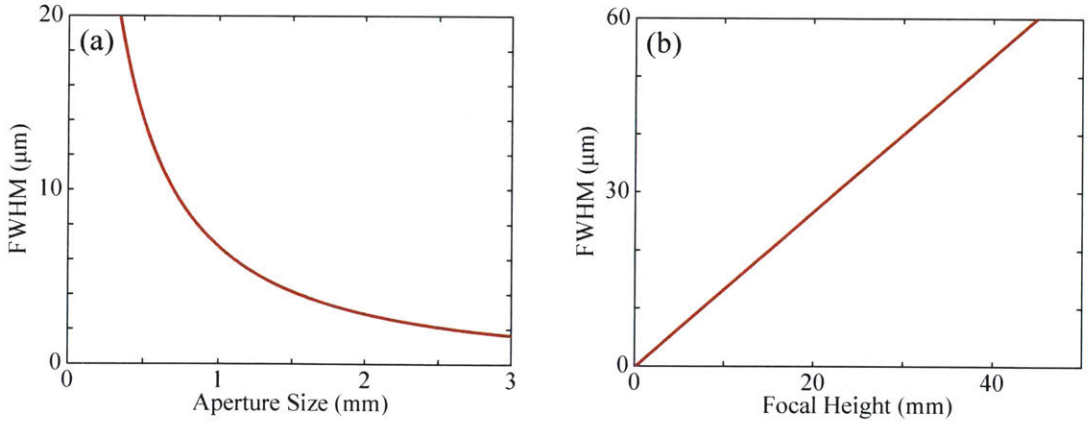

Figure 2.3: (a) Simulated power full-width half-maximum (FWHM) versus aperture size for a focusing phased array with 5 mm focal height and 1550 nm wavelength. (b) Simulated power FWHM versus focal height for a focusing phased array with 1 mm aperture size and 1550 nm wavelength.

FWHM decreases with an inverse scaling. In contrast, as shown in Fig. 2.3b, as the desired focal height increases, the FWHM increases linearly. These relationships match with the well-known Rayleigh criterion derived from the Airy pattern which describes the resolution limit of an imaging system as $R \approx \lambda f/A$ where R is the spatial resolution (analogous to the FWHM). As such, for maximally-enhanced trapping at long focal heights, large aperture sizes are necessary.

2.3 Non-Linear Steering of Focusing Phased Arrays

One advantage of using integrated optical phased arrays for focusing and optical trapping is that phased arrays allow for dynamic steering on-chip to enable arbitrary tweezing of optical traps. In a standard phased array system, a linear phase gradient is applied to the antennas to steer the radiated beam in the far field [24–26, 29, 30]. However, when this conventional linear steering approach is applied to a focusing phased array, in addition to the desired steering in the array dimension, the steering induces an undesired offset in the focal height of the spot. As an example, an array with 512 antennas, 2 μm antenna pitch, 5 mm desired focal height, and 1550 nm wavelength is simulated as shown in Fig. 2.4a. When this array is steered to a 1.5 mm offset in the array dimension using linear steering as shown in Fig. 2.4b, the resulting focal spot is formed at $z = 4.19\,\text{mm}$. For optical trapping applications where the sample under test is often housed in a microfluidic channel [2, 7], this steering-induced shift in the focal height can prove detrimental.

Instead, the desired horizontal offset should be encoded directly in the focusing phase as follows. First, the distance from each antenna to the focal point, initially given in Eq. (2.2), can be modified as:

$$L_n = \sqrt{f_z^2 + \left[d\left(N/2 + 1/2 - n\right) + f_x\right]^2} \tag{2.4}$$

where f_z is the desired focal height and f_x is the desired focal offset. The necessary

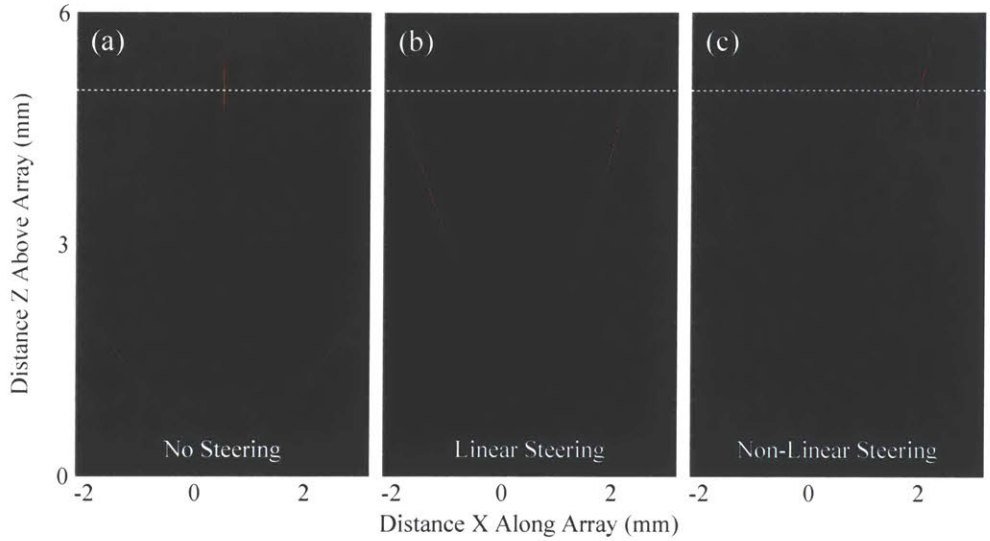

Figure 2.4: Simulated array-factor intensity above the array assuming (a) no steering, (b) linear steering, and (c) corrected non-linear steering. Simulated intensities are shown for an array with $f_x = 1.5\,\text{mm}$ offset, 512 antennas, $2\,\mu\text{m}$ antenna pitch, 5 mm focal height, and 1550 nm wavelength.

element phase distribution then follows directly from Eq. (2.3):

$$\Phi_n = \frac{2\pi}{\lambda}\left(L_1 - L_n\right). \tag{2.5}$$

Once again, this phase can be encoded modulo 2π. By applying this non-linear steering approach for $f_x = 1.5\,\text{mm}$, the focal spot is formed with the correct offset at the desired 5 mm focal height as shown in Fig. 2.4c. For comparison, the linear and non-linear steering phases are shown in Fig. 2.5 without 2π phase wrapping for clarity.

2.4 Conclusion

In this chapter, the element phase distributions necessary for generating focusing beams using phased arrays have been developed using a robust Fresnel-lens-inspired encoding. Discussion of the effects of the phase array parameters on the focus spot have been included with emphasis on the advantages of large aperture sizes. Additionally, the effects of conventional linear steering on the focal spot have been

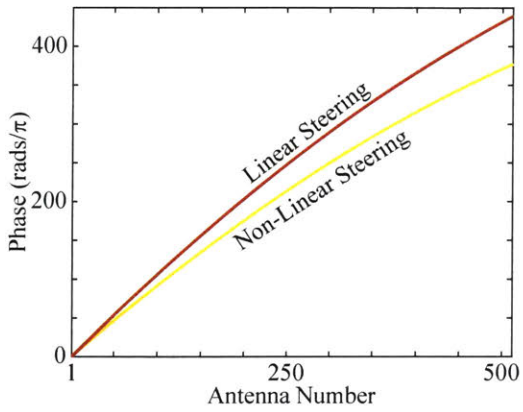

Figure 2.5: Element phase distribution for a focusing phased array with a $f_x = 1.5\,\text{mm}$ offset assuming linear steering (red) and corrected non-linear steering (yellow). Phase profiles are shown for an array with 512 antennas, $2\,\mu\text{m}$ antenna pitch, $5\,\text{mm}$ focal height, and $1550\,\text{nm}$ wavelength.

demonstrated and a non-linear steering approach has been developed. The developed focusing phased array theory will be utilized to demonstrate both one-dimensional and two-dimensional focusing integrated optical phased arrays in Ch. 6.

Chapter 3

Bessel-Beam Phased Array Theory

In this chapter, theory for generating quasi-Bessel beams is derived and discussed. First, an introduction to Bessel beams and their experimental approximations, Bessel-Gauss beams, is presented with discussion on applications and prior demonstrations. Next, the near-field theory developed in Ch. 2 is extended to derive the phases and amplitudes necessary for quasi-Bessel-beam generation using phased arrays. Additionally, discussion and simulations showing the effect of the array aperture and element parameters on the full-width half-maximum (FWHM) and Bessel length of the generated beam are included.

3.1 Introduction to Bessel-Beam Generation

Bessel beams, first discovered in 1987 [37], exhibit many interesting and useful properties including non-diffraction [37,38], self-healing [39], and optical pulling forces [40]. These beams enable propagation of a central beam with a finite width without diffraction-induced spreading [37,38].

However, Bessel beams are not experimentally realizable due to the infinite power and aperture necessary to generate a non-diffracting beam. Instead, by introducing a truncated-Gaussian envelope to the Bessel beam to place a finite limit on the power requirements, a new type of experimentally-realizable beam, the Bessel-Gauss beam, was developed to approximate a Bessel beam [37–39]. Within the Bessel length limit,

these quasi-Bessel beams have properties similar to physically-unrealizable Bessel beams, including an elongated central beam.

Due to their unique properties, Bessel-Gauss beams have contributed to a variety of important applications and advances [41]. For example, they have enabled multi-plane, multi-particle optical trapping [42], reduction of scattering and increases in depth of field in microscopy [43, 44], efficient laser lithography and fabrication [45], promotion of free-electron laser gain [46], improved laser corneal surgery [47], and adaptive free-space optical communications [48].

Bessel-Gauss beams are conventionally generated using a bulk optics approach wherein an Axicon lens (a conical glass prism) is illuminated with a truncated Gaussian beam to produce a Bessel-Gauss beam at the output [39]. Moreover, recent work has turned towards generation of Bessel beams in a more compact form factor. For example, Bessel-Gauss beam generation has been demonstrated using spatial light modulators [49], Dammann gratings [50], slit-groove structures [51], and meta-surfaces [52, 53] as shown in Fig. 3.1.

However, these demonstrations do not provide full on-chip integration and most are fundamentally limited to static beam formation. Integrated optical phased arrays provide one solution for generating quasi-Bessel beams in a fully-integrated, compact-form-factor system.

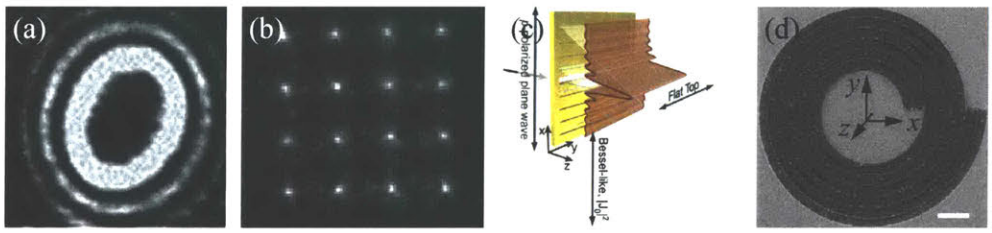

Figure 3.1: Overview of select compact-form-factor quasi-Bessel-beam-generating demonstrations using (a) spatial light modulators (figure from [49]), (b) Dammann gratings (figure from [50]), (c) slit-groove structures (figure from [51]), and (d) meta-surfaces (figure from [52]).

3.2 Element Phase and Amplitude Derivation and Bessel-Beam Phased Array Simulations

If the antennas in a phased array are spaced with a uniform pitch, d, and fed with a Gaussian amplitude and a linear phase distribution (as shown in Figs. 3.2a–b), the array creates a steerable, diffracting Gaussian beam in the far field of the array. This Gaussian element amplitude distribution is given by

$$A_n = \exp\left(\frac{-4\ln(2)(n - N/2 - 1/2)^2}{(NA_0)^2}\right) \tag{3.1}$$

where A_n is the amplitude applied to the nth antenna, N is the total number of antennas in the array, and A_0 is the variable amplitude parameter such that the FWHM of the Gaussian is given by NA_0. Similar to Eq. 2.1, the near-field electric-field profile generated by this phased array can be approximated by summing the electric-field components of each element in the array:

$$E(x, y, z) \approx \sum_{n=1}^{N} E_n(x, y, z) \approx \sum_{n=1}^{N} A_n e^{-i(2\pi r_n/\lambda + \Phi_n)} \tag{3.2}$$

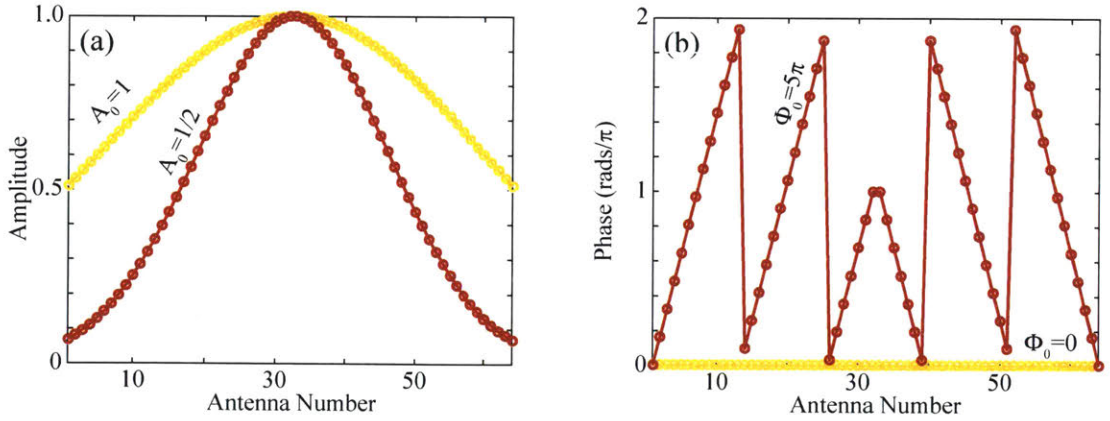

Figure 3.2: (a) Element amplitude distribution for a Gaussian-amplitude phased array with $A_0 = 1/2$ (red) and $A_0 = 1$ (yellow). (b) Element phase distribution for a standard (yellow) and Bessel (red) phased array with $\Phi_0 = 0$ and $\Phi_0 = 5\pi$, respectively. Phase and amplitude profiles and simulated intensities are shown for an array with 64 antennas, 10 μm antenna pitch, and 1550 nm wavelength.

where Φ_n is the phase applied to the nth antenna, r_n is the distance from the nth antenna to the point under consideration at coordinate (x, y, z), and λ is the propagation wavelength. Using this method, a Gaussian array with $A_0 = 1/2$, $N = 64$, and $d = 10\,\mu\text{m}$ is simulated; the generated intensity profile is shown in Fig. 3.3a.

In contrast, if an "Axicon-like" element phase distribution is applied in addition to the Gaussian amplitude, the array will generate a quasi-Bessel beam in the near field of the array. This Axicon phase is given by

$$\Phi_n = \Phi_0 \frac{-|n - N/2 - 1/2| + N/2 - 1/2}{N/2 - 1} \tag{3.3}$$

where Φ_n is the phase applied to the nth antenna and Φ_0 is the variable phase parameter. This phase can be encoded modulo 2π as shown in Fig. 3.2b. The simulated intensity profiles generated by three one-dimensional Bessel-beam arrays with varying parameters, Φ_0 and A_0, are shown in Figs. 3.3b–d. As shown in Fig. 3.3d, if the FWHM of the Gaussian element amplitude distribution is too large compared to the aperture size of the array, the integrity of the Bessel-Gauss beam is compromised –

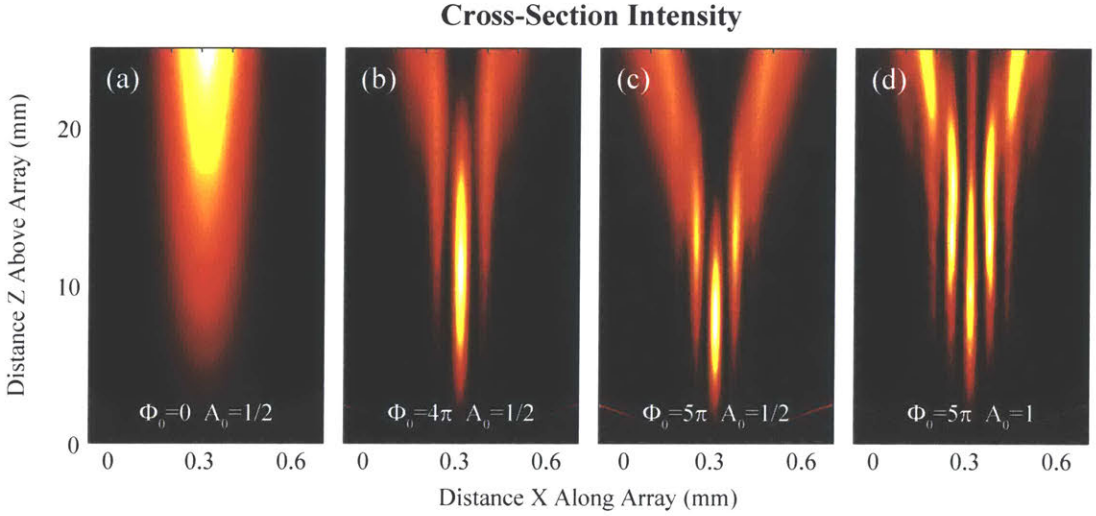

Figure 3.3: Simulated array-factor intensity above the array for a (a) Gaussian array with $\Phi_0 = 0$ and $A_0 = 1/2$, (b) Bessel array with $\Phi_0 = 4\pi$ and $A_0 = 1/2$, (c) Bessel array with $\Phi_0 = 5\pi$ and $A_0 = 1/2$, and (d) distorted Bessel array with $\Phi_0 = 5\pi$ and $A_0 = 1$. Simulated intensities are shown for an array with 64 antennas, $10\,\mu\text{m}$ antenna pitch, and 1550 nm wavelength.

the beam formed in Fig. 3.3d is degraded compared to a similar beam in Fig. 3.3c. Additionally, due to discretization of the continuous Bessel theory on an array with $d > \lambda/2$, higher-order grating lobes, which also exhibit Bessel properties, are generated by the array at larger angles (not shown in the simulation window), similarly to the high-order focusing grating lobes discussed in Sec. 2.1.

3.3 Parameters and Limits of Bessel-Beam Phased Arrays

For potential applications, two valuable figures of merit of a quasi-Bessel-beam generating array are the power FWHM of the central radiated beam and the Bessel length. Here, the FWHM is calculated in the plane where the power of the central beam is maximally enhanced, and the Bessel length is defined to the point above the array at which the central beam is overcome by the second-order beams and the Bessel approximation breaks down.

Similar to bulk implementations, these variables depend on the aperture size of the array and the maximum variation of the Axicon phase, Φ_0. As shown in Figs. 3.4a–b, as the array aperture size increases, the FWHM increases linearly while the Bessel length exhibits quadratic growth. In contrast, as shown in Figs. 3.4c–d, the FWHM and the Bessel length both are related to the phase parameter, Φ_0, through power-law scalings. As such, when considering the application space of the Bessel-generating device, it is important to consider the trade-offs between a long Bessel length versus a small FWHM. For example, if the device is proposed for simultaneous trapping of multiple small particles at varying heights, both a small FWHM and a long Bessel length are desired.

Similar to focusing-beam generation, Bessel-beam generation using phased arrays is limited to the Fresnel region (i.e. the near field) of the phased array, $r_{near} \approx A^2/\lambda$ where $A = Nd$ is the aperture size, as given by antenna theory [36]. Consequently, by increasing the array aperture size, the possible Bessel length of the array quadratically

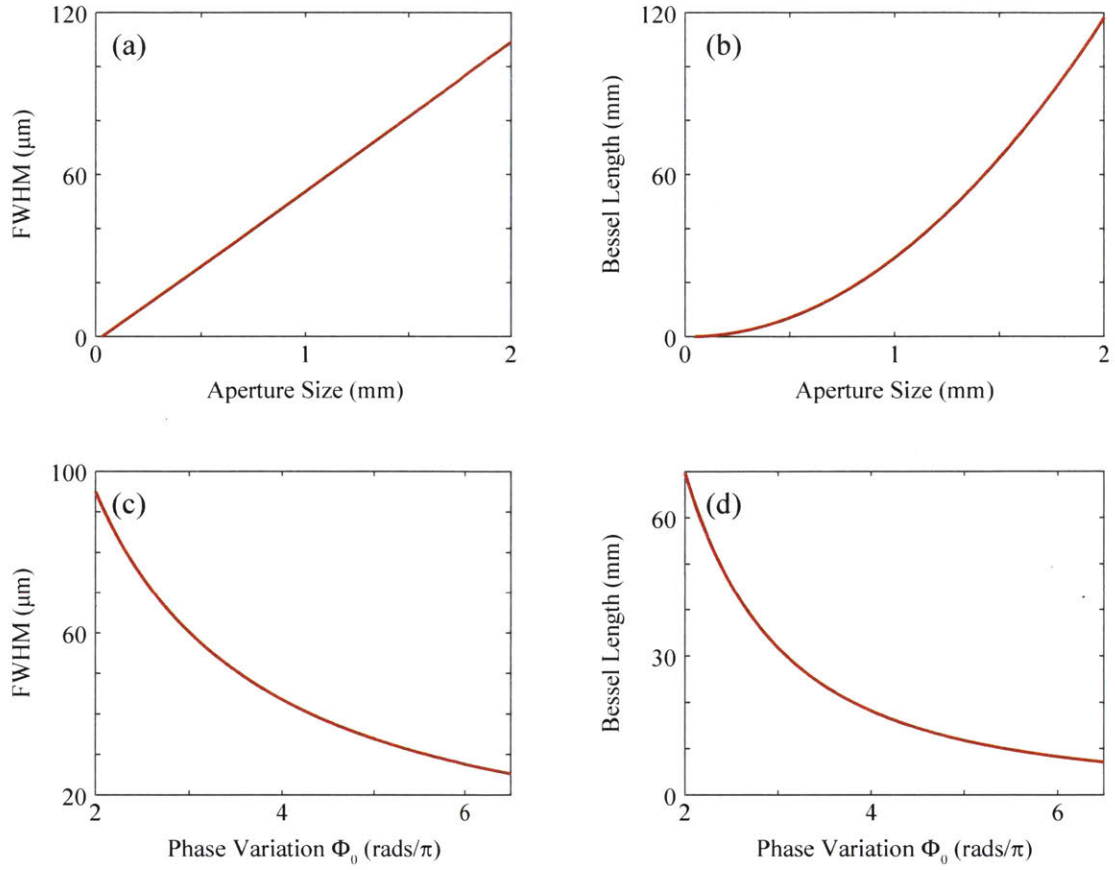

Figure 3.4: Simulated (a) power full-width half-maximum (FWHM) and (b) Bessel length versus array aperture size for an array with $\Phi_0 = 5\pi$, $A_0 = 1/2$, and 1550 nm wavelength. Simulated (c) FWHM and (d) Bessel length versus maximum element phase variation, Φ_0, for an array with 64 antennas, 10 μm antenna pitch, $A_0 = 1/2$, and 1550 nm wavelength.

increases.

3.4 Conclusion

In this chapter, the element phase and amplitude distributions necessary for generating Bessel-Gauss beams using phased arrays have been developed analogous to conventional bulk optics approaches. Additionally, the effects of the array aperture and element parameters on the full-width half-maximum (FWHM) and Bessel length of the generated beam have been presented and discussed. The developed Bessel-beam phased array theory will be utilized to demonstrate both one-dimensional and two-

dimensional quasi-Bessel-beam-generating integrated optical phased arrays in Ch. 7.

Chapter 4

Splitter-Tree-Based Integrated Optical Phased Array Architecture

In this chapter, a one-dimensional splitter-tree-based integrated optical phased array architecture is proposed and developed in both a silicon and a silicon-nitride platform for experimentally demonstrating near-field focusing and quasi-Bessel-beam-generating optical phased arrays. First, overviews of the splitter-tree-based architecture and the CMOS-compatible foundry fabrication processes are presented. Next, the various integrated nanophotonic components of the systems – including edge couplers, splitter networks, amplitude-control devices, passive phase-control structures, and grating-based antennas – are developed, numerically simulated, and experimentally demonstrated.

4.1 Overview of the One-Dimensional Splitter-Tree-Based Phased Array Architecture

A splitter-tree-based phased array architecture is based on a one-dimensional array of antennas. The power inputted into the system is evenly split into N channels using a splitter tree network comprised of symmetric 1-to-2 splitters. At the output of the splitter tree network, the amplitude and phase for each channel are set to enable

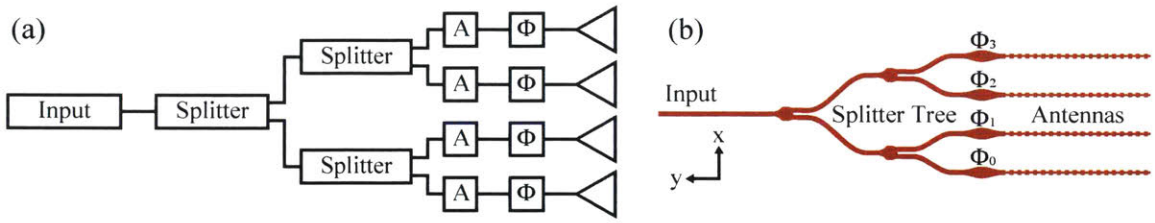

Figure 4.1: (a) Schematic of a four-antenna splitter-tree-based phased array architecture with arbitrary amplitude and phase control. (b) Schematic of an example splitter-tree-based focusing phased array integrated implementation.

arbitrary feeding of an array of N antennas. This process is shown in Fig. 4.1a.

In the utilized integrated platform, each step within the proposed phased array architecture is performed using a suite of nanophotonic devices. At the system input, an edge coupler or a grating coupler is used to couple light onto the chip. The splitter tree network is formed using a set of splitting devices, either multi-mode-interference or Y-junction splitters, and routing waveguides [23, 35]. Next, amplitude control is achieved using tap couplers and phase is controlled passively using either phase tapers or phase bumps. Finally, a variety of long grating-based antennas with varying characteristic – including exponentially radiating, focusing, and uniform emission – can be used to manipulate the light in the second dimension of the array and form a full two-dimensional aperture. An example implementation of a splitter-tree-based integrated phased array is shown in Fig. 4.1b.

4.2 Overview of the Foundry Fabrication Processes

The proposed phased arrays and accompanying device test structures are fabricated in a variety of CMOS-compatible foundry processes at CNSE SUNY. Specifically, three different platforms are used: a silicon platform, a silicon-nitride platform, and a custom-height silicon platform, as shown in Fig. 4.2.

In the silicon platform, 300 mm silicon-on-insulator (SOI) wafers with 2 μm buried oxide (SiO_2) thickness and a standard 220-nm-thick silicon (Si) device layer are used and patterned using 193 nm immersion lithography. Similarly, a non-standard custom-height silicon-on-insulator platform is also used with a 380-nm-thick silicon

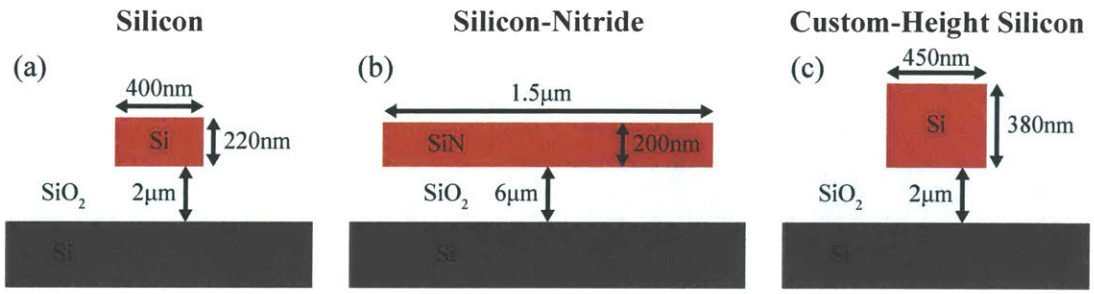

Figure 4.2: Schematic of the nominal single-mode waveguides in the (a) silicon, (b) silicon-nitride, and (c) custom-height silicon platforms (the buried oxide thickness is not shown to scale).

device layer. Finally, in the silicon-nitride platform, similar 300 mm silicon wafers are used with 6 μm buried oxide thickness. A 200-nm-thick silicon-nitride device layer with 1.95 refractive index at a 1550 nm wavelength is deposited using a plasma-enhanced chemical vapor deposition process and patterned using 193 nm immersion lithography.

These state-of-the-art CMOS-compatible platforms, coupled with multiple dopant, metal, and trench layers, have enabled a suite of advanced nanophotonic devices including modulators, distributed-feedback semiconductor lasers, phase shifters, de-

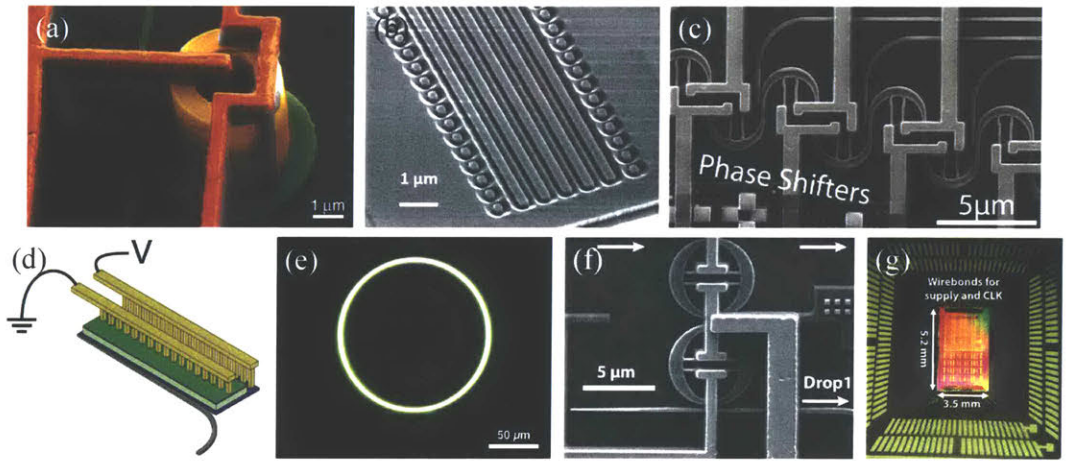

Figure 4.3: Overview of select device demonstrations in the CNSE SUNY foundry platform including (a) modulators (figure from [54]), (b) distributed-feedback lasers (figure from [55]), (c) phase shifters (figure from [30]), (d) detectors (figure from [56]), (e) ring lasers (figure from [57]), (f) higher-order filters (figure from [58]), and (g) wafer-scale 3D-bonded electronics (figure from [59]).

tectors, ring lasers, and higher-order filters, as well as wafer-scale 3D-bonding to electronics, as shown in Fig. 4.3 [30, 54–59]. In this work, the standard-height silicon and the silicon-nitride platform are used for the splitter-tree-based architecture while the pixel-based architecture (discussed in Ch. 5) uses the standard-height and the custom-height silicon platforms. By using these CMOS-compatible platforms for both architectures, the systems are naturally scalable to active demonstrations with wafer-scale 3D-bonded electronics [59] and monolithically-integrated laser sources [55] for fully-integrated and steerable chip-based optical trapping systems.

4.3 Fiber-to-Chip Coupling: Edge Couplers

At the input to the splitter-tree-based system, an on-chip edge coupler is used to efficiently couple laser light from an off-chip lensed fiber to the on-chip input waveguide. As shown in Fig. 4.4, an edge coupler is an inverse-taper structure [60]. At the chip facet, the edge coupler has a narrow width such that the optical mode is not well confined in the waveguide and closely matches the relatively-large 6.5 μm mode field diameter of the input fiber. The edge coupler then adiabatically tapers up to the single-mode waveguide width wherein the field is well confined in the fundamental transverse-electric mode.

For the 220-nm-height silicon-based systems, the edge couplers are designed with a 140 nm input width, 400 nm waveguide width to insure transverse-electric single-mode operation, and 150 μm total length to ensure an adiabatic transition from the input width. Similarly, for the 200-nm-height silicon-nitride-based systems, the edge couplers are designed with a 320 nm input width, 1.5 μm waveguide width, and 300 μm total length and, for the 380-nm-height silicon-based systems, a 120 nm input width,

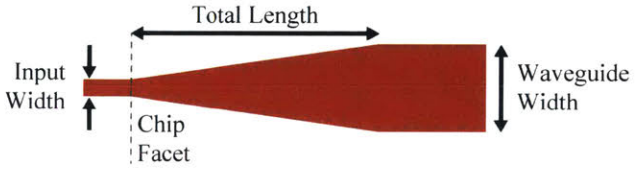

Figure 4.4: Schematic of an edge coupler.

450 nm waveguide width, and 150 μm total length are used.

As a different method for fiber-to-chip coupling, record-efficiency grating couplers with unidirectional and Gaussian-mode-matched operation have been investigated [61–63]. However, since grating couplers are inherently more bandwidth limited and are not as fabrication tolerant, edge couplers are used throughout this work.

4.4 Splitter Networks

Next, after the edge coupler, the input waveguide is split into N waveguide arms using a set of cascaded 1-to-2-waveguide splitting devices with even splitting ratios to evenly distribute the input power to the multiple waveguide arms (as developed in [23, 35]). In this work, the silicon-nitride-based networks use multi-mode-interference splitters, as discussed in Sec. 4.4.1, while Y-junction splitters were used for the silicon-based networks, as discussed in Sec. 4.4.2. Additionally, either 90° waveguide bends or sinusoidal-shaped bends are designed to reduce bending radiation loss while routing between the splitter devices as discussed in Sec. 4.4.3.

4.4.1 Multi-Mode-Interference Splitters

Silicon-nitride multi-mode-interference (MMI) splitters present one method for evenly distributing power within the splitter network of a splitter-tree-based phased array architecture [23]. As shown in Fig. 4.5a, an MMI is a symmetric, 1-to-2-waveguide splitting device based on self-imaging principals [64]. To ensure even splitting with high-efficiency, a commercially-available finite-difference time-domain (FDTD) solver is used to rigorously simulate the device and optimize its geometry for low insertion loss and coupling into the symmetric mode output.

As shown in Fig. 4.5b, by setting the MMI length to 28.7 μm with a 7 μm MMI width and 2.5-μm-wide input and output waveguides, the simulated and measured insertion losses at the design wavelength are found to be 0.04 dB and less than 0.1 dB, respectively [23]. Additionally, since it is desirable for the last layer of the splitter network to have to small waveguide pitch to reduce grating lobes (as discussed in

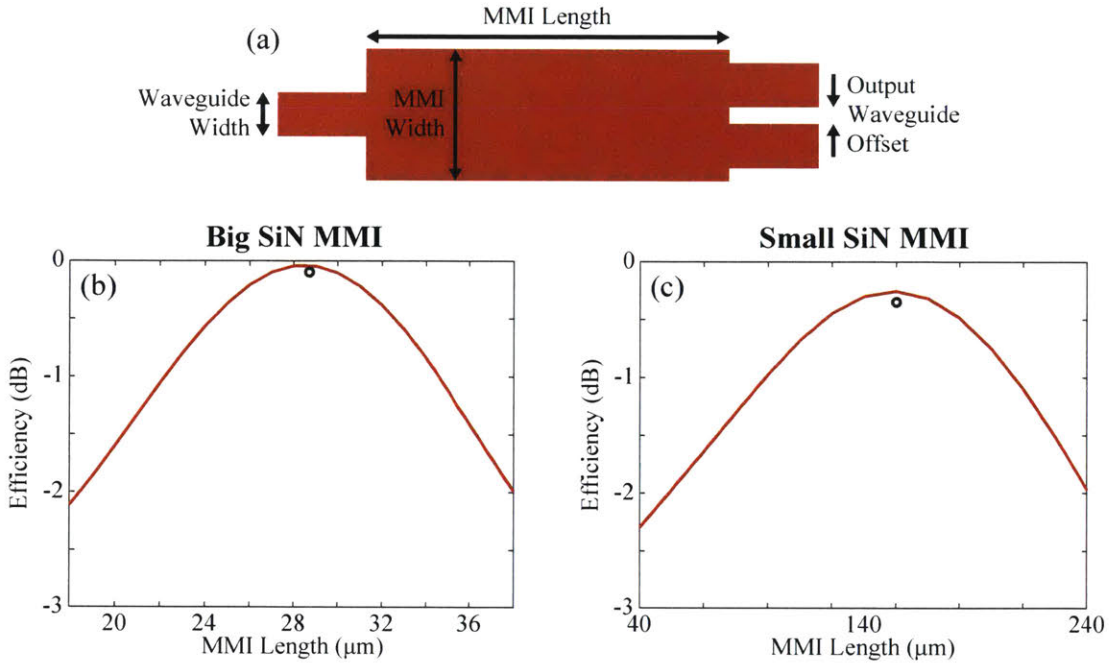

Figure 4.5: (a) Schematic of a multi-mode-interference (MMI) splitter. Simulated (red) and measured (black) efficiency versus MMI device length for a (b) big and (c) small silicon-nitride MMI [23].

Sec. 2.1), a smaller MMI is designed to be used in the last layer within the splitting network [23]. By setting the smaller MMI length to 16 μm with a 5 μm MMI width and 1.6-μm-wide input and output waveguides, the simulated and measured insertion losses of this smaller MMI at the design wavelength are found to be 0.27 dB and ~0.35 dB, respectively, as shown in Fig. 4.5c [23].

4.4.2 Y-Junction Splitters

Similarly to the MMI splitters, a Y-junction device can be used to evenly distribute power within the splitter network of a splitter-tree-based phased array architecture. Compared to the MMI splitters, a Y-junction device can be optimized to be shorter while demonstrating comparable insertion losses and, therefore, can be more space efficient.

In this work, silicon Y-junctions, as shown in Fig. 4.6 and developed in [65], are used for the silicon-based splitter networks. The Y-junctions have 500-nm-wide input

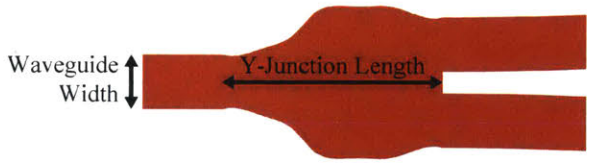

Figure 4.6: Schematic of a Y-junction splitter as developed in [65].

and output waveguides and are only 2 μm long. In the CNSE process, the insertion loss of this splitter is measured to be ~0.15 dB [35].

4.4.3 Waveguide Routing

To route between the output of each splitter device to the input of the next layer of splitters, a network of routing waveguides is used in a configuration similar to the schematic shown in Fig. 4.1a. However, unlike electronic wiring, the bend radii of the waveguides in the network need to be designed such that the radiation losses due to the waveguide bends and the mode mismatch between the straight waveguides and the bent waveguides are reduced. Figure 4.7a shows the mode overlap between the fundamental mode in a straight waveguide and the radiating mode within a bent waveguide for varying bend radius in both the silicon and silicon-nitride platforms as simulated using a mode solver. As shown, as the radius of the bend decreases, the mode overlap between the straight waveguide mode and the bent mode is reduced. Similarly, as the bend radius decreases, the propagation loss in the bent waveguide increases. As shown, this effect has a more dominate manifestation in the silicon-nitride platform due to the low index contrast between the 1.95-index silicon-nitride and the 1.45-index oxide cladding. As such, in the silicon and the silicon-nitride splitter networks, the minimum waveguide bending radii used are limited to 5 μm and 200 μm, respectively. To meet this limitation while keeping a compact footprint, a mixture of 90° bends and sinusoid-shaped bends are used for routing [23, 35].

Additionally, similar to electronic circuits, if the waveguides in an integrated photonics system are placed too close together, evanescent crosstalk between waveguide arms occurs. To quantify this crosstalk, the full power transfer length between two

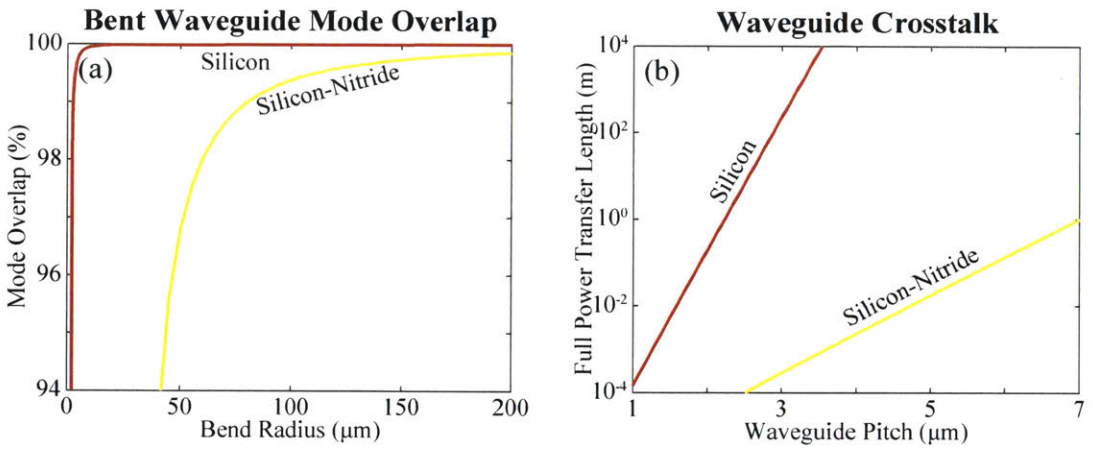

Figure 4.7: (a) Simulated mode overlap of a bent waveguide compared to a straight waveguide versus bend radius for silicon (red) and silicon-nitride (yellow). (b) Simulated full power transfer length versus waveguide pitch for two silicon waveguides (red) and two silicon-nitride waveguides (yellow).

waveguides is calculate. First, a mode solver [66] is used to simulate the symmetric and anti-symmetric modes in a pair of waveguides and obtain their propagation coefficients. Next, these propagation coefficients are used to calculate the full power transfer length as follows:

$$L_{transfer} = \frac{\pi}{2\left(\beta_{sym} - \beta_{anti-sym}\right)} \tag{4.1}$$

where β_{sym} and $\beta_{anti-sym}$ are the propagation coefficients of the symmetric and the anti-symmetric modes, respectively. Figure 4.7b shows this full power transfer length versus waveguide pitch in the silicon and silicon-nitride platforms. As the pitch between the waveguides decreases, the full power transfer length gets smaller. As such, given that the proposed splitter-tree-based arrays use long antennas on the order of 1 mm long, the pitches of the last layer of the silicon and the silicon-nitride splitter trees are limited to 2 μm and 4 μm, respectively, to reduce crosstalk between the antennas while limiting the number of undesired grating lobes.

4.5 Amplitude Control: Tap Couplers

At the output of the splitter tree, a tap coupler structure (shown in Fig. 4.8a) can be placed on each waveguide arm to enable amplitude control in the splitter-tree-based architecture as schematically shown in Fig. 4.1a. A tap coupler couples a percentage of the light from each waveguide arm to a tap port while the remainder of the light in the thru port is routed off the chip. Similar to the crosstalk discussed in Sec. 4.4.3, the coupling between the input port and the tap port is a result of the evanescent coupling between the bus waveguide and the tap waveguide. As such, this coupling can be controlled by appropriately setting the coupling gap and the coupling length.

To design these coupling gaps and lengths, the tap coupler is rigorously simulated using an FDTD solver. Figure 4.8b shows the resulting power coupling versus the coupling gap assuming a 0 μm coupling length; as expected, by decreasing the coupling gap, the coupling increases. Similarly, Figure 4.8c shows the power coupling

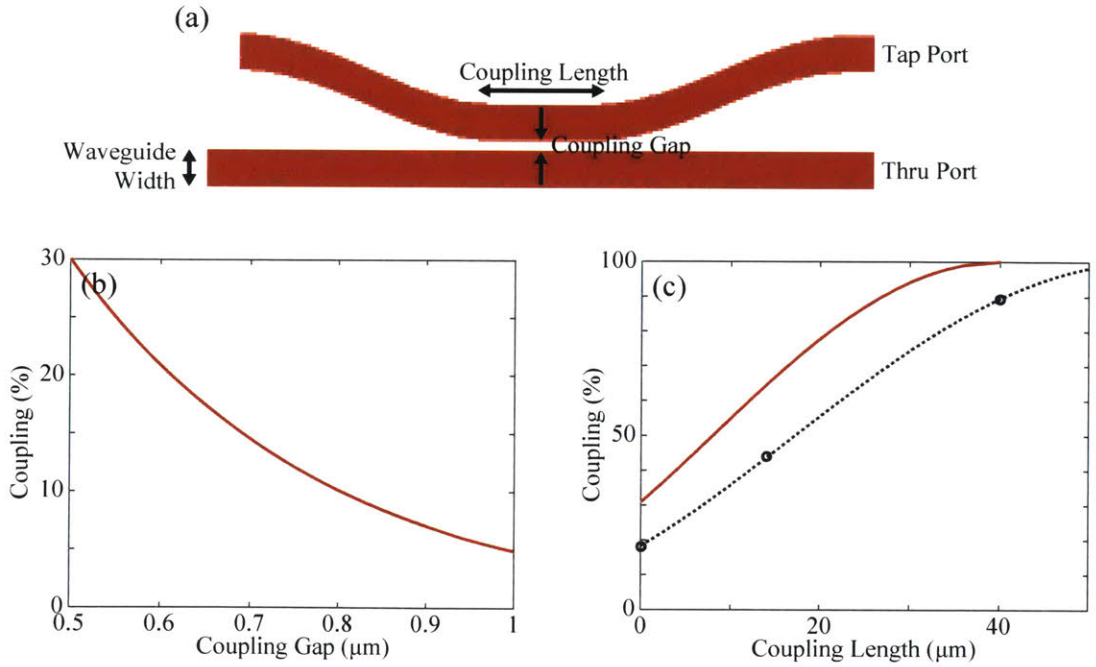

Figure 4.8: (a) Schematic of a tap coupler device. (b) Simulated coupling versus coupling gap assuming 0 μm coupling length for a silicon-nitride tap coupler. (c) Simulated (red) and measured (black) coupling versus coupling length assuming a 500 nm coupling gap for a silicon-nitride tap coupler.

versus the coupling length assuming a 500 nm coupling gap; as expected, by increasing the length of the coupling region, the input power is sinusoidally coupled from the thru port into the tap port of the device. Additionally, fabricated test structures with varying coupling lengths are used to experimentally validate the performance of the device. As shown in Fig. 4.8c, the experimental results confirm the sinusoidal coupling relationship; however, due to the low tolerance of the device and fabrication imperfections, an imperfect performance is seen which can be improved in future fabrication iterations. As such, the length and gap of each waveguide arm's tap coupler in the array can be chosen to enable a variety of amplitude feeding profiles to the antennas, including the Gaussian profile, given by Eq. (3.1), necessary for Bessel-Gauss-beam generation.

4.6 Phase Control

On the output tap port of each coupler device, a phase control device is placed to enable arbitrary phase encoding to each antenna in the array. In this work, both passive phase tapers (discussed in Sec. 4.6.1) and phase bumps (discussed in Sec. 4.6.2) are used to enable static phase encoding, although future scaling to active-control using phase shifters is available using the same fabrication platforms [67].

4.6.1 Phase Tapers

First, phase tapers are developed as one method for arbitrary passive phase control. A phase taper structure (shown in Fig. 4.9a) imparts a static phase delay dependent on the length of the device's wide section. If the length of the wide section of the structure is increased while the total length is kept constant, the relative phase induced by the structure increases linearly. To quantify this relationship, a mode solver [66] is used to simulate the fundamental modes in the standard waveguide width and in the device's wide section to obtain the effective refractive index of each mode. Next, the effective

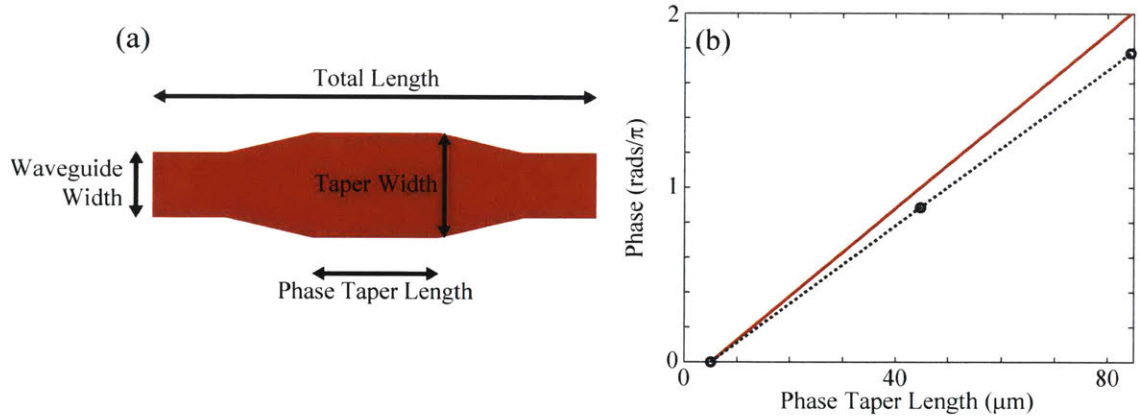

Figure 4.9: (a) Schematic of a phase taper device. (b) Simulated (red) and measured (black) relative phase versus length of the 2.2-μm-wide section of the silicon-nitride phase taper.

indeces are used to calculate the relative phase induced as follows:

$$\Phi = \frac{2\pi}{\lambda}\left(L_{WG}n_{eff,WG} + L_{taper}n_{eff,taper}\right) \tag{4.2}$$

where λ is the free-space propagation wavelength, L_{WG} and L_{taper} are the lengths of the narrow and wide sections of the device, respectively, and $n_{eff,WG}$ and $n_{eff,taper}$ are the effective indices of the narrow and wide sections, respectively.

To confirm this relationship, a silicon-nitride phase taper is rigorously simulated using an FDTD solver. The standard 1.5 μm width is tapered up to and down from the 2.2-μm-width wide section of the device using a 50-μm-long taper. The wide section of the structure is then increased while the total length is kept at a constant 185 μm. The simulated relative phase induced by the structure is shown in Fig. 4.9b. Additionally, fabricated interferometer-based test structures with varying phase lengths are used to experimentally validate the performance of the device. As shown in Fig. 4.9b, the experimental data closely matches the expected performance. As such, the phase length of each waveguide arm's phase taper in the array can be chosen to enable a variety of phase feeding profiles to the antennas, including the "Fresnel" and "Axicon" profiles, given by Eq. (2.3) and Eq. (3.3), necessary for focusing-beam and Bessel-Gauss-beam generation.

4.6.2 Phase Bumps

Similarly to the phase tapers, a phase bump device (shown in Fig. 4.10a) can also be placed on each waveguide arm to impart a static phase delay and passively control the feeding phase in a splitter-tree-based phased array architecture. However, phase bumps present an advantage over phase tapers since they enable similar phase encoding while encompassing a smaller footprint. Specifically, a phase bump adiabatically increases the width of the waveguide from the nominal waveguide width to a variable wider width using a sinusoidal shape while keeping the length of the device constant. At the output of the device, a static phase delay dependent on the variable width is induced.

To enable phase control in both the standard-height silicon and silicon-nitride platforms, two phase bump structures are rigorously designed using an FDTD solver. The silicon phase bump structure is designed to interface to the nominal 400 nm waveguide width. The length of the structure is chosen to be 6 μm to reduce undesired excitation of higher-order modes while keeping a compact form factor. Figure 4.10b

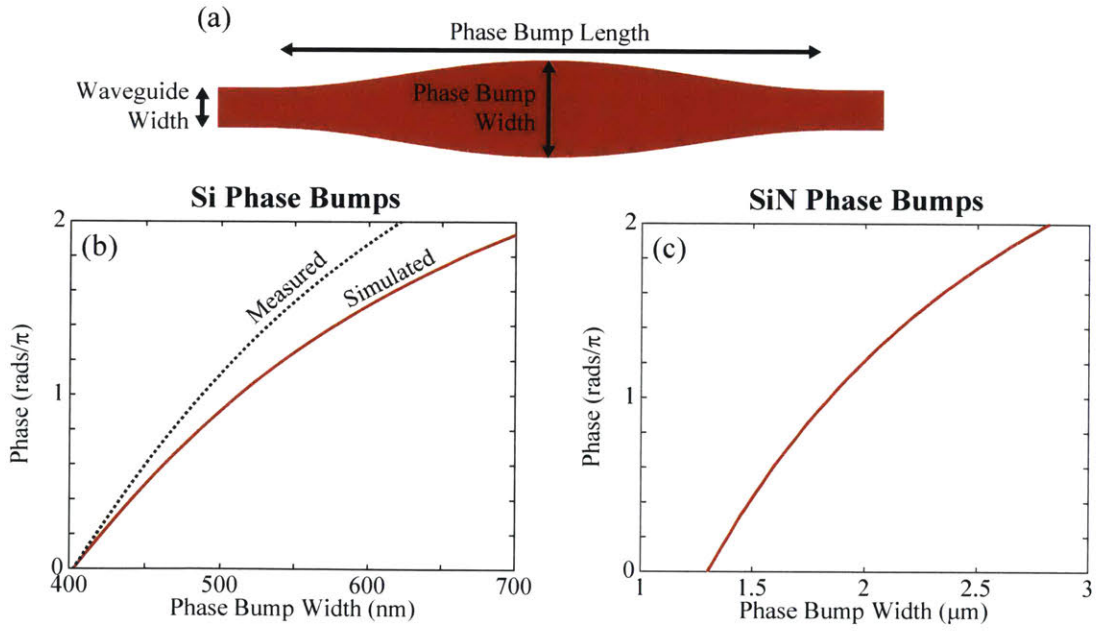

Figure 4.10: (a) Schematic of a phase bump device. (b) Simulated (red) and measured (black) relative phase versus phase bump width for the silicon phase bump. (c) Simulated relative phase versus phase bump width for the silicon-nitride phase bump.

shows the simulated and measured relative phase versus phase bump width (the experimental data is obtained using fabricated interferometer-based test structures similar to the fabricated phase taper tests as described in Sec. 4.6.1). As expected, as the width of the phase bump is increased, the relative phase induced by the structure increases. Similarly, a silicon-nitride phase bump structure is designed starting at the nominal 1.5 μm waveguide width with a 75 μm total length. The resulting simulated relative phase versus phase bump width are shown in Fig. 4.10c. As expected, the phase bump structure is able to impart a full 2π phase encoding in less than half the length of the silicon-nitride phase taper structure. Similarly to the phase tapers, the width of each waveguide arm's phase bump in the array can be chosen to enable a variety of feeding phase profiles to the antennas, including the "Fresnel" and "Axicon" profiles, given by Eq. (2.3) and Eq. (3.3), necessary for focusing-beam and Bessel-Gauss-beam generation. Additionally, due to the modulo 2π phase encoding, the architecture is very robust to any phase variations due to fabrication.

4.7 Antennas

Finally, after each phase structure, a long grating-based antenna is placed on each arm to create a large quasi-two-dimensional aperture using the one-dimensional splitter-tree-based architecture as shown schematically in Fig. 4.1a. In this work, a variety of antennas are used with varying characteristics. First, standard, exponentially-radiating antennas (as developed and demonstrated in [23, 30]) are proposed as one solution in Sec. 4.7.1. However, these antennas were original developed for formation of beams in the far field of the array such that the light radiated out of the array is not focused in the near field in the antenna dimension. As such, additional grating-based antennas are developed to focus light in the antenna dimension; silicon and silicon-nitride focusing antennas are demonstrated in Sec. 4.7.2 and a silicon-nitride focusing antenna with uniform emission is developed in Sec. 4.7.3.

4.7.1 Exponentially-Radiating Antennas

Standard grating-based antennas (as shown in Fig. 4.11a) present one solution for emitting light out of the phased array with a quasi-two-dimensional aperture. The antennas are designed to radiate out of the plane of the chip and exponentially along the antenna length by periodically perturbing the waveguide [23, 30]. By varying this symmetric inward perturbation of the antenna, the rate of this exponentially radiation – i.e. the scattering strength defined as the power radiated by the antenna per unit length – can be controlled.

To quantify this scattering strength and design the antennas, an FDTD solver is used to rigorously simulate a standard silicon antenna. A 610 nm nominal antenna width is chosen to reduce grating lobes in the antenna dimension [30]. Next, as the antenna perturbation is increased, the period of the antenna is adjusted correspondingly to insure that the optical path length of one period of the antenna remains the same and the antenna continues to radiate at approximately 90° out of the plane of the chip.

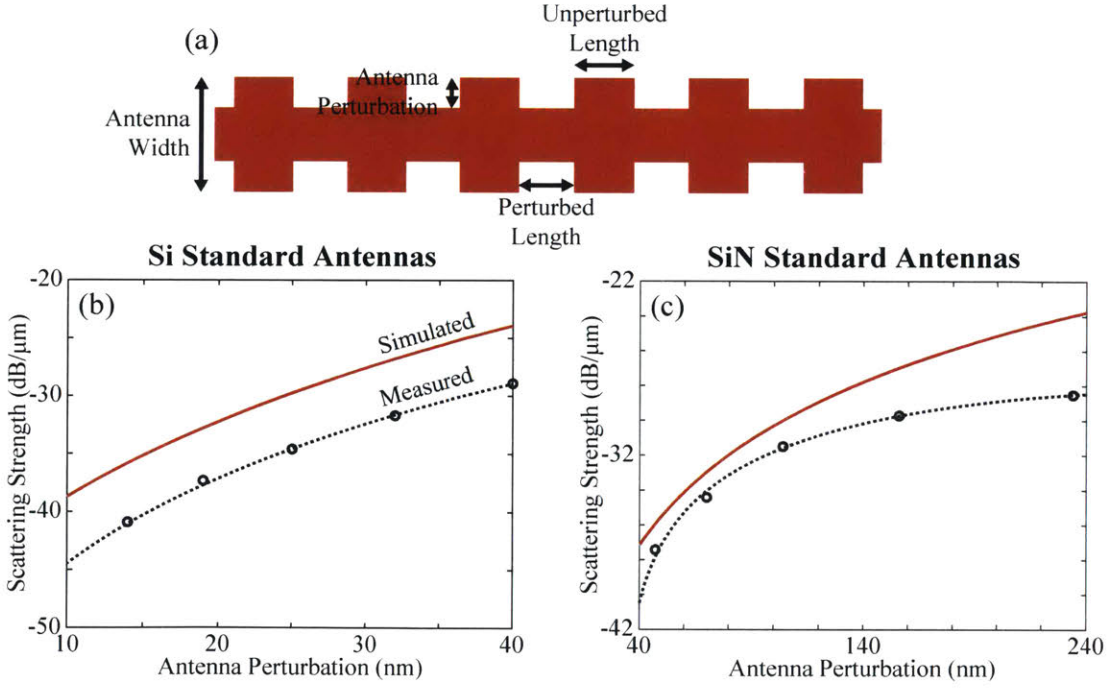

Figure 4.11: (a) Schematic of a grating-based antenna. Simulated (red) and measured (black) scattering strength versus antenna perturbation for the (b) standard silicon antenna [30] and (c) standard silicon-nitride antenna [23].

The resulting simulated scattering strength as a function of the antenna perturbation, as well as the corresponding experimental data, is shown in Fig. 4.11b. Similarly, the scattering strength versus perturbation is simulated and experimentally measured for a 1.5-μm-wide silicon-nitride antenna as shown in Fig. 4.11c [23]. As expected, as the perturbation of both antennas is increased, more light is scattered and the scattering strength increases. However, the experimental data exhibits some discrepancies when compared to the simulated results – the measured scattering strength is, in general, lower than the simulated scattering strength – which can be attributed to fabrication imperfections and can be further improved in future fabrication iterations.

As such, for a given antenna length, the perturbation can be chosen to reduce the excess power lost at the end of the antenna. For example, a 156 nm perturbation is used for the 1.2-mm-long silicon-nitride antennas in Sec. 6.2, a 178 nm perturbation is used for the 0.65-mm-long silicon-nitride antennas in Sec. 7.1, and a 30 nm perturbation is used for the 0.9-mm-long silicon antennas in Sec. 6.3.

4.7.2 Focusing Antennas

Next, to enable focusing in the antenna dimension, silicon and silicon-nitride focusing antennas are developed. By appropriately adiabatically chirping the period of a grating-based antenna along the antenna length, the radiation angle along the antenna can be varied such that the device focuses light above the chip. This process is similar to adiabatic synthesis of locally periodic vertical grating couplers with varying radiation angles [61, 63, 68].

To implement this synthesis, the relative phase induced by a period unit cell of the antenna is simulated in FDTD as the length of the wider, unperturbed section of the antenna is varied and the length of the narrower, perturbed section is kept constant as shown in Figs. 4.12a and 4.12c. The silicon antenna is simulated with a 30 nm perturbation and a 310 nm perturbed section length. Similarly, the silicon-nitride antenna is simulated with a 156 nm perturbation and a 500 nm perturbed section length. The unit cells for each antenna type are then chosen and concatenated such that the synthesized phase follows the unwrapped phase given by Eq. (2.3).

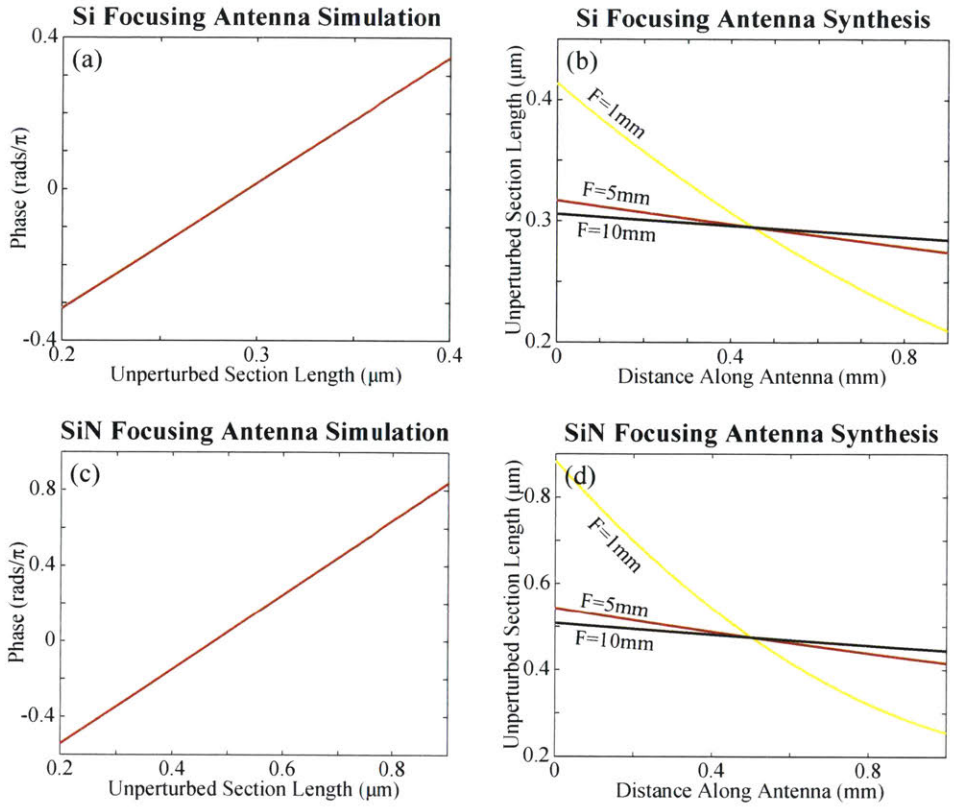

Figure 4.12: Simulated relative phase versus length of the unperturbed section of the (a) silicon and (c) silicon-nitride antenna. Synthesized unperturbed section length versus distance along the (b) silicon and (d) silicon-nitride antenna necessary for focusing at 1 mm (yellow), 5 mm (red), and 10 mm (black). Simulated and synthesized plots are shown for a silicon antenna with 30 nm perturbation and 310 nm perturbed length and a silicon-nitride antenna with 156 nm perturbation and 500 nm perturbed length.

The synthesized lengths for focusing at 1 mm, 5 mm, and 10 mm above the chip for both the silicon and silicon-nitride antennas are shown in Figs. 4.12b and 4.12d, respectively. Note that lengths of 295 nm and 475 nm are chosen as the reference phase points for the silicon and silicon-nitride antennas, respectively, during the synthesis since, at those points, the antennas radiate upwards with a slight angle. Although this introduces a slight angle offset to the focusing in the antenna dimension, it ensures that the antennas do not induce undesired back reflections through the Bragg condition.

4.7.3 Focusing Antennas with Uniform Emission

As a third antenna option for the splitter-tree-based architecture, a silicon-nitride focusing antenna with uniform emission is developed. For both the standard antennas discussed in Sec. 4.7.1 and the focusing antennas developed in Sec. 4.7.2, the perturbation of the antenna is kept constant along the antenna length such that the scattering strength of each period of the antenna is approximately equal and the antenna emits with an exponentially-decaying profile. However, to optimize the performance of the array at the focal plane, either a uniform or a Gaussian amplitude profile in the plane of the chip is desired. As such, a uniform-emission focusing antenna is developed and synthesized by adiabatically chirping both the period and the perturbation of the grating-based antenna along its length.

To implement this synthesis, first, the desired radiation angle and scattering strength of the antenna along its length are derived. The desired radiation angle along the antenna length is given as

$$\theta(y) = \arctan\left(\frac{l_{ant}/2 - y}{f_z}\right) \tag{4.3}$$

where l_{ant} is the total length of the antenna, y is the distance along the antenna, and f_z is the desired focal height. Similarly to beam shaping of the scattering strength in grating couplers [62,69], the desired scattering strength for uniform emission in an antenna is derived as

$$\alpha(y) = \frac{1}{l_{ant} - y}. \tag{4.4}$$

The resulting desired radiation angle and scattering strength as a function of the distance along the antenna assuming a 1 mm length and 5 mm focal height are shown in Figs. 4.13a–b.

Next, a portion of the antenna is simulated in FDTD as the antenna perturbation and the unperturbed section of the antenna are varied while the length of the perturbed section is kept at a constant 500 nm. The resulting two-dimensional design plots for the radiation angle and scattering strength calculated from the FDTD

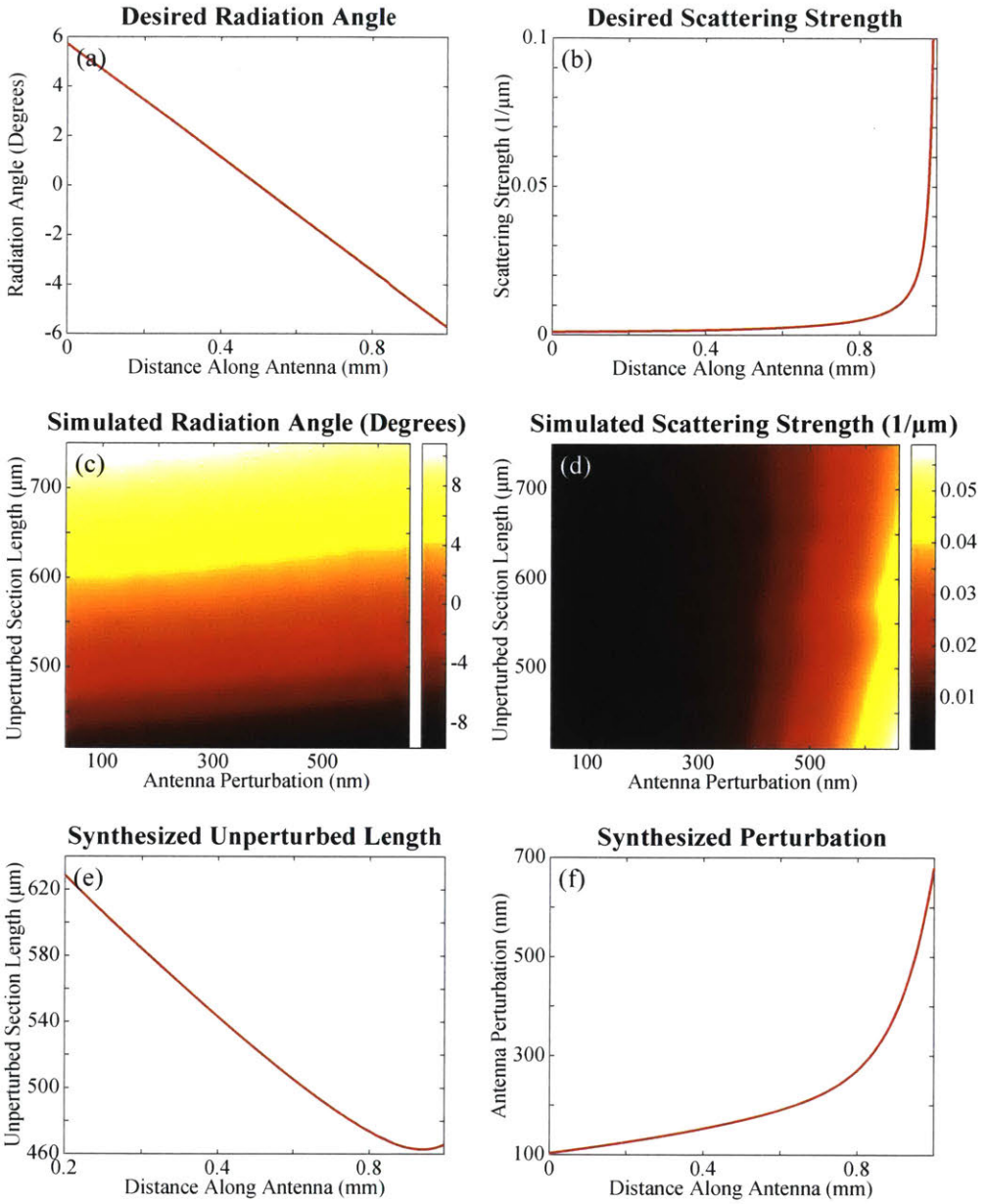

Figure 4.13: Desired (a) radiation angle and (b) scattering strength versus distance along the antenna for a uniform-emission focusing antenna with 5 mm focal height. Simulated (c) radiation angle and (d) scattering strength for varying antenna perturbation and unperturbed section length for a silicon-nitride antenna with 500 nm perturbed length. Synthesized (e) unperturbed section length and (f) antenna perturbation for a silicon-nitride uniform-emission focusing antenna with 5 mm focal height.

simulation sweep are shown in Figs. 4.13c–d.

Finally, using these two-dimensional design plots, the unit cells are then cho-

sen and concatenated such that a uniform-emission focusing antenna is synthesized. Specifically, for each period of the antenna, the unperturbed section length and perturbation are chosen such that the desired simulated radiation angle and scattering strength at that point in the antenna are obtained. Figures 4.13e–f show the synthesized unperturbed section length and perturbation for a 1-mm-long silicon-nitride antenna with a 5mm focal height.

4.8 Conclusion

In this chapter, a one-dimensional splitter-tree-based integrated optical phased array architecture has been developed in both silicon and silicon-nitride platforms for demonstrating near-field focusing and quasi-Bessel-beam-generating optical phased arrays. A one-dimensional splitter-tree-based phased array architecture used for far-field beam forming [23,35] has been modified to passively encode arbitrary phase and amplitude distributions to the elements of the array. Discussion has been presented on the utilized platforms, the input coupling, and the devices and waveguide routing in the splitter-tree-network. A variety of nanophotonic components have been numerically simulated and experimentally demonstrated for amplitude and phase control including tap couplers, phase tapers, and phase bumps. Additionally, exponentially-radiating and uniform-emission focusing antennas have been developed, simulated, and synthesized. This architecture presents one method for implementing the focusing and Bessel theory developed in Ch. 2 and Ch. 3, respectively, and is used throughout Ch. 6 and Ch. 7 to experimentally demonstrate near-field focusing and quasi-Bessel-beam-generating phased arrays.

Chapter 5

Pixel-Based Integrated Optical Phased Array Architecture

In this chapter, a two-dimensional pixel-based integrated optical phased array architecture in both the standard-height and the non-standard-height silicon platform is proposed as a second method for experimentally demonstrating near-field focusing and quasi-Bessel-beam-generating optical phased arrays. First, overviews of the pixel-based architecture and the CMOS-compatible foundry fabrication processes are presented. Next, the various integrated nanophotonic components of the systems – including directional couplers, adiabatic bends, delay lines, and grating-based emitters – are reviewed and numerically simulated.

5.1 Overview of the Two-Dimensional Pixel-Based Phased Array Architecture

A pixel-based phased array architecture is based on a two-dimensional array of antennas. The input to the system is split into M rows using a set of M row pixels which couple light from the input into each row. Next, on each row, M emitter pixels are used to couple from each the row into M antennas. This creates an array aperture of $M \times M$ antennas as shown in Fig. 5.1a.

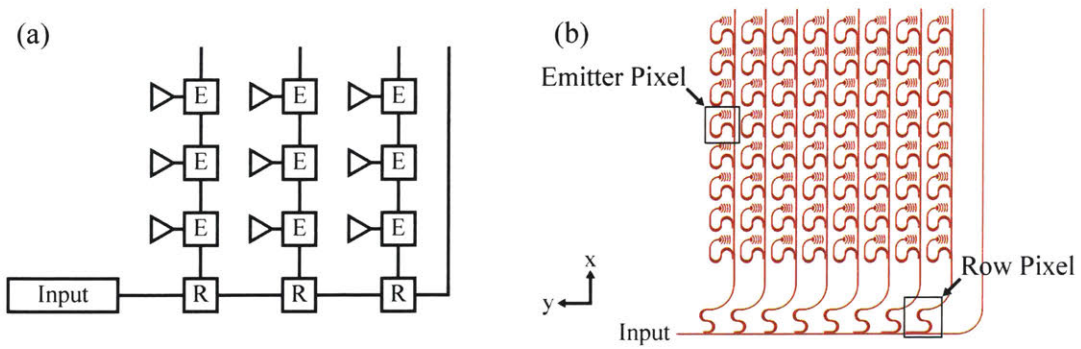

Figure 5.1: (a) Schematic of a nine-antenna pixel-based phased array architecture with arbitrary amplitude and phase control using row and emitter pixels. (b) Schematic of an example pixel-based quasi-Bessel-beam-generating phased array implementation.

In the developed integrated platform, each step within the architecture is performed using a suite of nanophotonic devices as developed in [25]. At the system input, an edge coupler or a grating coupler is used to couple light onto the chip as discussed in Sec. 4.3. Both the row pixels and the emitter pixels are designed with the same topology; a directional coupler is used for amplitude control, two adiabatic bends are used to enable a compact footprint and small antenna pitch, and delay lines are used for phase control. Finally, compact grating-based emitters within each emitter pixel are used to radiate light and form a two-dimensional aperture. An example implementation of a pixel-based integrated phased array is shown in Fig. 5.1b.

The pixel-based phase array architecture and accompanying device test structures are also fabricated in a CMOS-compatible foundry process at CNSE SUNY on a 300 mm silicon-on-insulator (SOI) wafer with 2 μm buried oxide thickness using 193 nm immersion lithography as described in Sec. 4.2. However, for most demonstrations, the non-standard 380-nm-thick silicon device layer is used (compared to the standard 220 nm thickness used in previous demonstrations [25, 70]) which requires redesign of all photonic components in the system.

5.2 Amplitude Control: Directional Couplers

Within each row and emitter pixel, a directional coupler (shown in Fig. 5.2a) is used for amplitude control [25]. By increasing the length of the coupling region of the device or decreasing the coupling gap, the percentage of power coupled either from the input waveguide to the row waveguide or from the row waveguide to the emitter is varied similarly to the tap coupler in the splitter-tree-based architecture in Sec. 4.5.

To design these coupling gaps and lengths, the directional coupler is rigorously simulated using an FDTD solver. Figure 5.2b shows the resulting power coupling versus the coupling length for the 220 nm platform assuming a 150 nm gap between the coupler and the waveguide. Similarly, Figure 5.2c shows the power coupling versus the coupling length for the 380 nm platform assuming a 120 nm coupling gap. As expected, by increasing the length of the coupling region, the input power is sinusoidally coupled from the thru port into the tap port of the device.

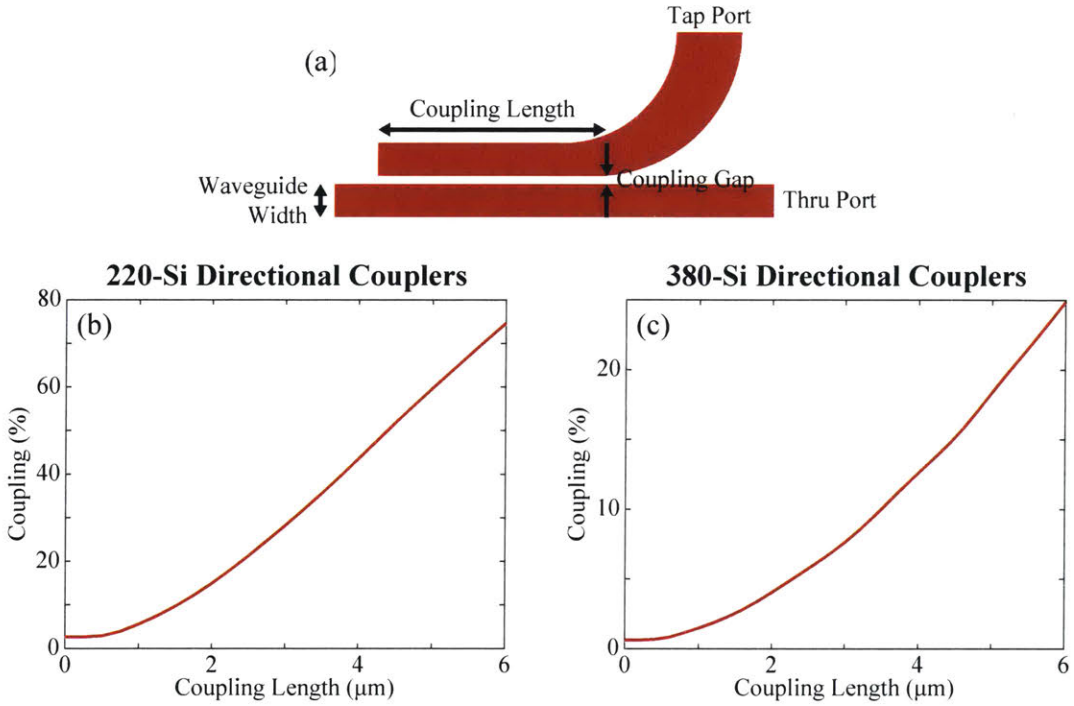

Figure 5.2: (a) Schematic of a directional coupler within a row or emitter pixel [25]. Simulated coupling versus coupling waveguide length for (b) the 220-nm-height directional coupler with a 150 nm coupling gap and (d) the 380-nm-height directional coupler with a 120 nm coupling gap.

To enable a desired arbitrary near-field emission from the array, the power coupling coefficient for the emitter pixel in the (m, n) unit cell is set to [70]

$$\eta_{mn} = \frac{A_{mn}^2}{A_{mN}^2 + \sum_{j=n}^{N} A_{mj}^2} \tag{5.1}$$

where η_{mn} is the coupling coefficient for the n^{th} emitter pixel in the m^{th} row, M is the total number of rows, N is the total number of emitters in each row, and A_{mn} is the desired amplitude element amplitude for the (m, n) antenna in the array. Similarly, the power coupling coefficient for the m^{th} row pixel is set to [70]

$$\eta_m = \frac{A_{mN}^2 + \sum_{j=1}^{N} A_{mj}^2}{A_{MN}^2 + \sum_{j=1}^{N} A_{Mj}^2 + \sum_{i=m}^{M} \left(A_{iN}^2 + \sum_{j=1}^{N} A_{ij}^2 \right)}. \tag{5.2}$$

Using this formalism, the length of each directional coupler in the array can be chosen to enable a variety of amplitude feeding profiles to the antennas, including the uniform emission necessary for focusing-beam generation and the Gaussian profile, given by Eq. (3.1), necessary for Bessel-Gauss-beam generation. Discussion on simplification of the coefficient encodings for each array type are given in Ch. 6 and Ch. 7.

5.3 Phase Control

After each directional coupler, as shown in Fig. 5.3a, two compact adiabatic curves are placed and the offset length between them is varied to allow for arbitrary phase control to each row or emitter [25]. This architecture allows for full phase control independent of the position of the antenna while keeping a compact footprint and enabling direct scaling to an active demonstration.

5.3.1 Adiabatic Bends

For direct scaling to a tunable architecture, adiabatic bends are used within each row and emitter pixel as described in [67, 70]. In summary, for efficient thermo-optic phase shifting, it is advantageous to directly integrate silicon heaters within the routing waveguide. However, the silicon leads necessary for this integration can scatter the light and cause loss. As such, by adiabatically increasing the width of the waveguide in the bend, the field can be confined to the outer edge of the bend (as shown in Fig. 5.3b) such that the leads can interface to the inner edge to enable a direct, low-loss contact to the device [67].

In this work, adiabatic bends are developed for both the 220-nm-height and the 380-nm-height silicon platform. The bends are rigorously simulated using an FDTD

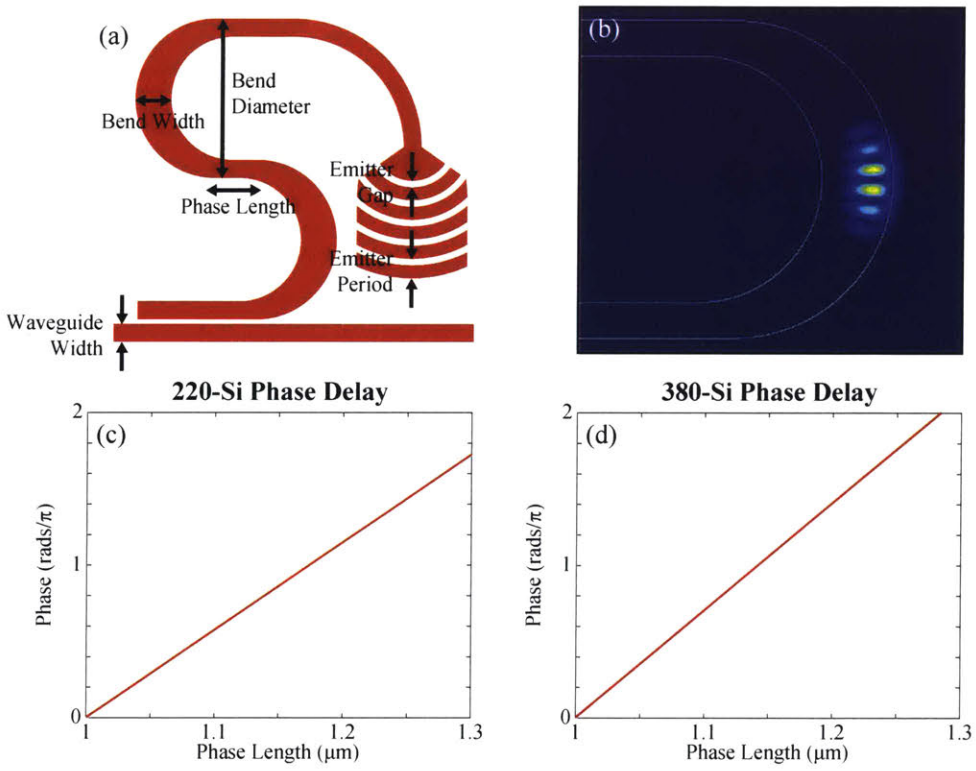

Figure 5.3: (a) Schematic of an emitter pixel with adiabatic bends and phase delay line labeled. (b) Simulated electric-field in a 380 nm-height adiabatic waveguide bend. Simulated relative phase versus phase waveguide length for the pixel-based architecture unit cell in (c) the 220-nm-height platform and (d) the 380-nm-height platform.

solver to optimize their bend diameters and bend widths to ensure low-loss performance while enabling a 10 μm pixel pitch. For the 220 nm platform, a 4 μm bend diameter and a 950 nm bend width are used while a 4 μm bend diameter and a 900 nm bend width are used for the 380 nm platform.

5.3.2 Delay Lines

Next, the offset between the two adiabatic curves (i.e. the length of the delay lines) is varied to enable arbitrary passive phase control for each pixel within the array [25]. Specifically, the position of the second bend is varied while keeping the position of the first bend and the antenna constant such that the phase encoding does not cause undesired shifts in the position of the antennas within the array. The induced relative phase versus the offset phase length is simulated using an FDTD solver and confirmed using a mode solver (similar to the technique developed in Sec. 4.6.1). Figures 5.3c–d show the resulting phase versus offset length for the 220-nm-height and the 380-nm-height silicon platforms, respectively. As such, the phase offset delay lines of each pixel in the array can be chosen to enable a variety of phase feeding profiles to the antennas, including the "Fresnel-like" encoding, given by Eq. (2.3), necessary for focused-beam generation and the "Axicon-like" profile, given by Eq. (3.3), necessary for Bessel-Gauss-beam generation.

Additionally, to ensure correct operation, these phase encodings must be modified to compensate for the variable phase induced by the directional couplers within the array [70]. As the length of the coupling region of a directional coupler is varied, a slight phase variation, dependent on the coupling length, is induced in both the tap and thru ports [71]. Although the variation due to one directional coupler is relatively small compared to the necessary phase encodings, this variation compounds in larger pixel numbers. To account for this compounding variable phase, the phase encoding for the m^{th} row is modified to

$$\Phi_{m,encoding} = \Phi_m - \Phi_{m,tap} - \sum_{j=1}^{m-1} \Phi_{j,thru} \tag{5.3}$$

where $\Phi_{m,encoding}$ is the modified phase encoded into the m^{th} row pixel's phase delay lines, Φ_m is the desired phase for the m^{th} row pixel, $\Phi_{m,tap}$ is the phase induced in the tap port of the m^{th} row pixel's directional coupler, and $\Phi_{m,thru}$ is the phase induced in the thru port of the m^{th} row pixel's directional coupler. Similarly, the desired phase encoding for the emitter pixel in the (m, n) unit cell is modified to

$$\Phi_{mn,encoding} = \Phi_{mn} - \Phi_{mn,tap} - \sum_{j=1}^{n-1} \Phi_{mj,thru} \tag{5.4}$$

where $\Phi_{mn,encoding}$ is the modified phase encoded into the (m, n) emitter pixel's phase delay lines, Φ_{mn} is the desired phase for the (m, n) emitter pixel, $\Phi_{mn,tap}$ is the phase induced in the tap port of the (m, n) emitter pixel's directional coupler, and $\Phi_{mn,thru}$ is the phase induced in the thru port of the (m, n) emitter pixel's directional coupler. As such, the row pixels are programmed to compensate for the phase induced by the row pixels' directional couplers while the emitter pixels are programmed to compensate for the phase induced by the emitter pixels' directional couplers.

5.4 Emitter Antennas

Finally, a compact grating-based emitter antenna (as shown in Fig. 5.3a) is placed in each emitter pixel within the pixel-based array architecture to radiate the light out of the plane of the chip. The emitter radiates light at a slight angle from vertical to reduce back reflection. For the 220-nm-height platform, the emitter developed in [25] is used while a similar design is developed using a rigorous FDTD solver with optimized dimensions for the non-standard 380-nm-height platform. Specifically, in the 220-nm-height design, each emitter antenna consists of 4 fully-etched circular grating teeth with a 728 nm period and a 483 nm gap between teeth and one partially-etched circular grating to break the vertical symmetry in the device [25]. Similarly, in the 380-nm-height design, each emitter antenna consists of 5 fully-etched grating teeth with a 490 nm period and a 172 nm gap between teeth.

5.5 Conclusion

In this chapter, a two-dimensional pixel-based integrated optical phased array architecture has been shown in two silicon platforms for demonstrating near-field focusing and quasi-Bessel-beam-generating optical phased arrays. Using the architecture developed in [25], a variety of nanophotonic components have been designed and numerically simulated, including directional couplers, adiabatic bends, phase delay lines, and grating-based emitters, and synthesis of the device parameters for arbitrary amplitude and phase control has been presented. This architecture presents a second method for implementing the focusing and Bessel theory developed in Ch. 2 and Ch. 3, respectively, and is used throughout Ch. 6 and Ch. 7 to experimentally demonstrate near-field focusing and quasi-Bessel-beam-generating phased arrays.

Chapter 6

Focusing Integrated Optical Phased Arrays

In this chapter, the splitter-tree-based and pixel-based phased array architectures are used to experimentally demonstrate focusing integrated optical phased arrays. First, the one-dimensional silicon-nitride splitter-tree-based architecture is implemented to demonstrate a 128-antenna integrated phased array with a $0.5\,\text{mm} \times 1.2\,\text{mm}$ aperture which focuses the radiated light in one-dimension to a line with a $\sim 13\,\mu\text{m}$ FWHM at a focal height of 5 mm. Next, the one-dimensional silicon splitter-tree-based architecture is implemented to demonstrate both 1D- and 2D-focusing 512-antenna integrated phased arrays with $1.024\,\text{mm} \times 0.9\,\text{mm}$ apertures which focus light down to $\sim 7\,\mu\text{m}$ and $\sim 2\,\mu\text{m}$ spots at focal heights of 5 mm and 1 mm above the chip, respectively. Additionally, experimental data showing wavelength steering of the focused spot in the antenna dimension is shown and discussion of extension of the architecture to electronic control in the array dimension is presented. Finally, the two-dimensional pixel-based architecture is utilized to show a second type of passive focusing phased array with capabilities for active electronic focusing in two dimensions. Specifically, a 1024-antenna variant with 32 rows by 32 columns and a $0.32\,\text{mm} \times 0.32\,\text{mm}$ aperture is demonstrated which focuses light to a $\sim 21\,\mu\text{m}$ spot 5 mm above the chip, and a 10,000-antenna variant with 100 rows by 100 columns and a $1\,\text{mm} \times 1\,\text{mm}$ aperture is demonstrated which focuses light to a $\sim 21\,\mu\text{m}$ spot 10 mm above the chip.

6.1 Characterization Setup

To characterize the fabricated arrays, a near-field optomechanical characterization setup is developed. First, the fabricated chip is placed on a mounting base with pitch-yaw-tilt mechanical controls as shown in Fig. 6.1a. Next, an off-chip 1550-nm-wavelength pigtail laser diode is connected to an attenuator and a fiber-based polarization controller. The output of the polarization controller is then connected to a 6.5 μm mode-field-diameter lensed fiber that is mounted on a tapered V-groove fiber holder on a NanoMax stage. Using the mechanical controls on the NanoMax stage, the pitch-yaw-tilt stage, and the polarization controller, the position of the lensed fiber and the polarization of the input light is optimized such that the laser light is maximally coupled into the transverse-electric mode of the device under test on the chip.

Next, an optical system is used to simultaneously image the plane of the chip onto a visible camera and an InGaAs IR camera using a Mitutoyo objective, shortpass dichroic mirror, and plano-convex lens as shown in Fig. 6.1b. The height of the optical imaging system is then progressively mechanically scanned using a microscope focus block such that top-down views of the intensity at varying heights above the chip are recorded. These top-down views are then integrated in the antenna or array dimension

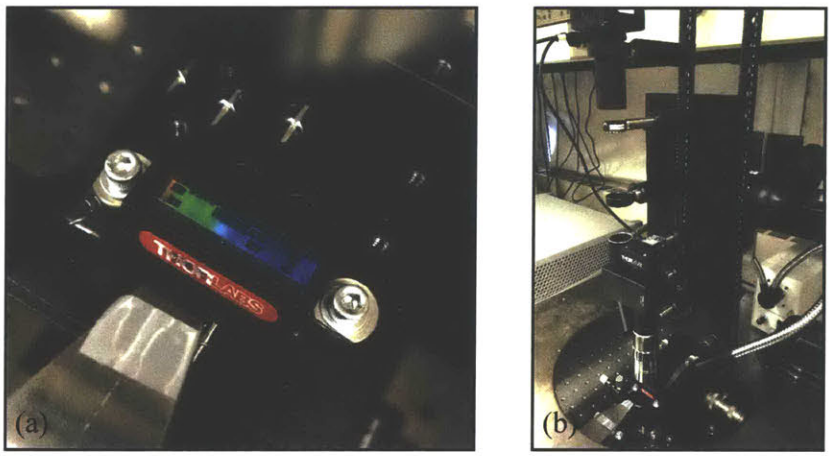

Figure 6.1: Photographs of (a) a fabricated integrated optical phased array chip on the near-field characterization setup and (b) the near-field characterization setup.

to visualize the cross-sectional intensity as a function of the distance above the chip.

6.2 Focusing Splitter-Tree-Based Phased Arrays in Silicon-Nitride

Foremost, a passive 1D-focusing integrated optical phased array is implemented and fabricated using the one-dimensional splitter-tree-based silicon-nitride architecture described in Ch. 4. The array focuses the radiated light in one-dimension to a line with a $\sim$13 µm FWHM at a focal height of 5 mm.

6.2.1 Implementation in the Splitter-Tree-Based Architecture

The fabricated 1D-focusing phased array utilizes the silicon-nitride one-dimensional splitter-tree architecture as developed in Ch. 4. A 7-layer multi-mode interference (MMI) splitter tree (see Sec. 4.4) is used to evenly distribute the input power to 128 waveguide arms with a final pitch of 4 µm. On each arm, a phase bump structure (see Sec. 4.6.2) is placed which imparts a static phase delay dependent on the width of the bump. The width of each bump is chosen so that the correct phase profile, given by Eq. (2.3), for focusing in the array dimension at 5 mm above the chip is applied

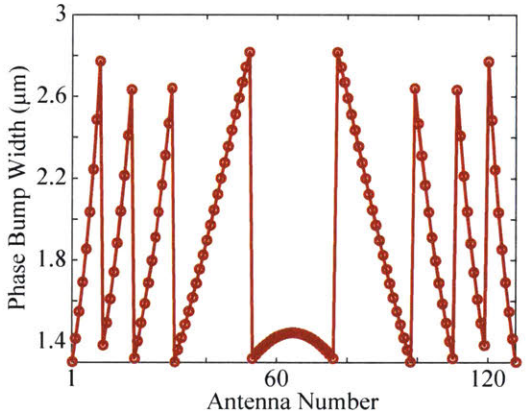

Figure 6.2: Synthesized phase bump width versus antenna number for a focusing silicon-nitride splitter-tree-based phased array with 128 antennas, 4 µm antenna pitch, 5 mm focal height, and 1550 nm wavelength.

as shown in Fig. 6.2. Finally, a 1.2-mm-long exponentially-radiating grating-based antenna (see Sec. 4.7.1) is placed on each arm to create a 0.5 mm × 1.2 mm aperture size.

6.2.2 One-Dimensional-Focusing Experimental Results

The resulting cross-sectional intensity as a function of the distance above the chip and three top-down views are shown in Fig. 6.3. In the plane of the chip (Fig. 6.3d), the aperture is illuminated by the antennas. As expected, the antennas radiate with a characteristic exponentially profile. As the system scans to the expected focal plane 5 mm above the chip (Fig. 6.3c), the light is tightly-focused in the array dimension. At this height, a FWHM of ~13μm is measured in the array dimension, x, matching

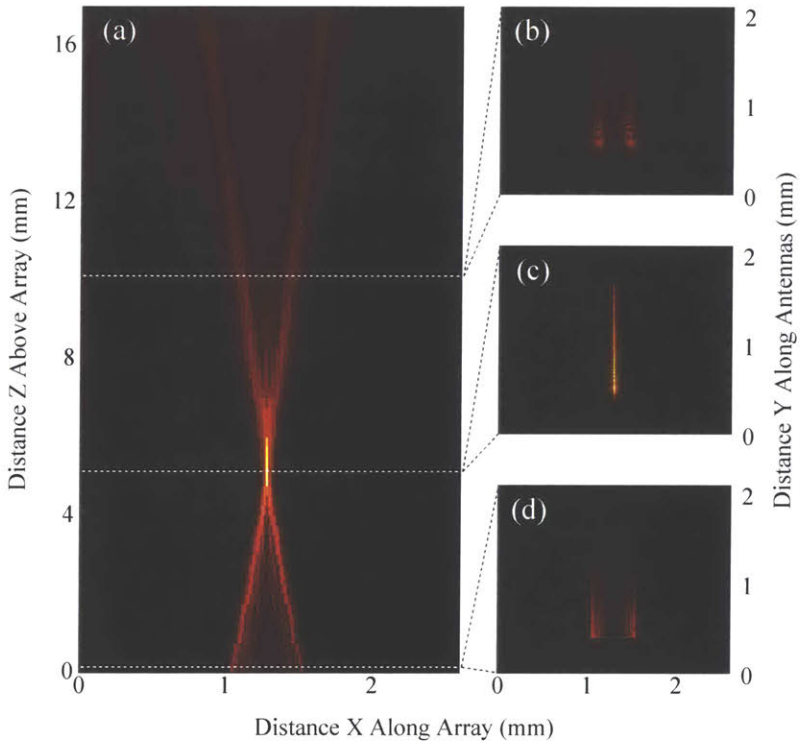

Figure 6.3: (a) Measured cross-sectional intensity (in dB) above the chip for a 1D-focusing silicon-nitride splitter-tree-based phased array with top-down intensity shown (d) in the plane of the chip, (c) at the focal plane, and (b) above the focal plane. Intensities are shown for an array with 128 antennas, 4 μm antenna pitch, 5 mm focal height, and 1550 nm wavelength.

the simulated value of 13μm. Finally, above the focal plane (Fig. 6.3b), the light is, once again, diffracted out.

6.2.3 Discussion of Extension to Active Tuning and Future Work

Since the array is fabricated in a CMOS-compatible platform, it is naturally scalable to an active arbitrarily-tunable system by interfacing with active silicon-based phase shifters [67]. Specifically, in place of the passive phase bump structures on each waveguide arm, a vertical layer-transition device can be used to transition from each silicon-nitride waveguide to a silicon waveguide, an adiabatic thermo-optic phase shifter can be placed on each arm, and the inverse layer transition can be utilized to return to the silicon-nitride layer to connect to the antennas.

Additionally, two-dimensional focusing can be achieved using this same silicon-nitride one-dimensional architecture by using silicon-nitride uniform-emission focusing antennas as developed in Sec. 4.7.3. Furthermore, the demonstration can be scaled to larger aperture sizes to further reduce the focus spot size and enable larger focal heights. For example, assuming the 4 mm aperture previously demonstrated in this silicon-nitride platform [23], a 3.3 μm spot size could be demonstrated 10 mm above the chip. Finally, since silicon-nitride has a higher bandgap than silicon [72], this array could be used for high-power applications at the designed 1550 nm wavelength [73] while a silicon array would be limited by two-photon absorption in this regime.

6.3 Focusing Splitter-Tree-Based Phased Arrays in Silicon

To remove the need for vertical layer transitions in future active demonstrations, the one-dimensional splitter-tree-based silicon architecture developed in Ch. 4 is implemented to demonstrate a variety of focusing phased arrays as shown in Fig. 6.4.

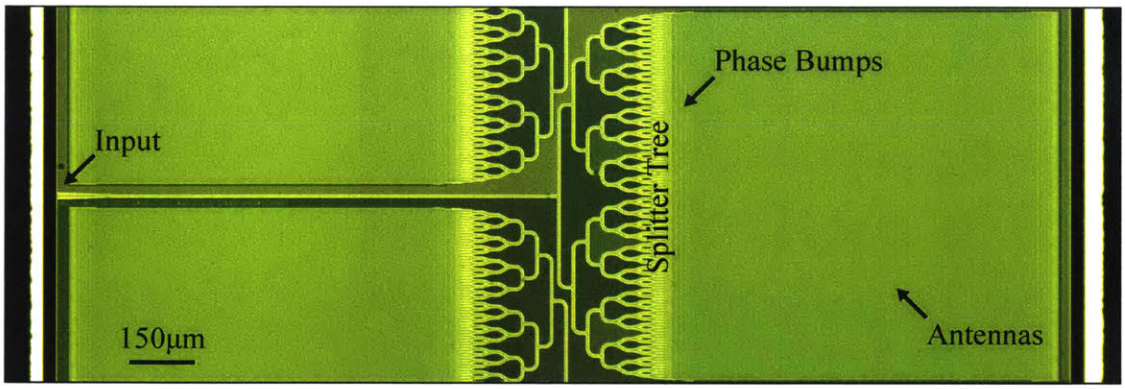

Figure 6.4: Micrograph of a fabricated splitter-tree-based focusing phased array with 512 antennas and 2 μm antenna pitch.

Results are shown for both 1D-focusing and 2D-focusing arrays with 1 mm and 5 mm focal heights. Additionally, experimental data showing wavelength steering of the focused spot in the antenna dimension is demonstrated and discussion of extension of the architecture to electronic control in the array dimension is presented.

6.3.1 Implementation in the Splitter-Tree-Based Architecture

The fabricated 1D- and 2D-focusing phased arrays utilize the silicon one-dimensional splitter-tree architecture as developed in Ch. 4. A 9-layer Y-junction splitter tree (see Sec. 4.4) is used to evenly distribute the input power to 512 waveguide arms with a final pitch of 2 μm. On each arm, a silicon phase bump structure (see Sec. 4.6.2) is placed which imparts a static phase delay dependent on the width of the bump. The width of each bump is chosen so that the correct phase profile, given by Eq. (2.3), for focusing in the array dimension at either 1 mm or 5 mm above the chip is applied as shown in Fig. 6.5. Finally, a 0.9 mm-long exponentially-radiating grating-based antenna is placed on each arm to create a 0.5 mm × 1.2 mm aperture size. For the 1D-focusing arrays, the antenna used is the standard, non-focusing silicon antenna (see Sec. 4.7.1), while, for the 2D-focusing arrays, the focusing silicon antenna (see Sec. 4.7.2) is used.

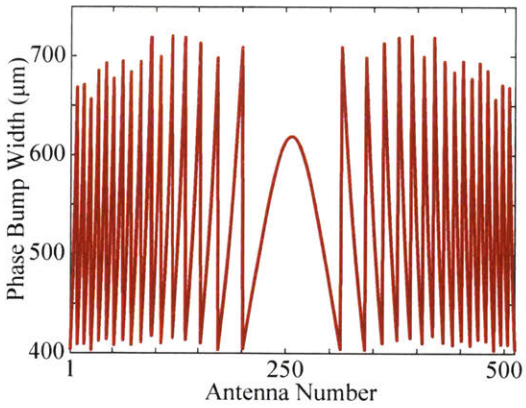

Figure 6.5: Synthesized phase bump width versus antenna number for a focusing silicon splitter-tree-based phased array with 512 antennas, 2 μm antenna pitch, 5 mm focal height, and 1550 nm wavelength.

6.3.2 1D- and 2D-Focusing Experimental Results

The resulting cross-sectional intensity as a function of the distance above the chip and three top-down views are shown in Figs. 6.6a–e for the fabricated splitter-tree-based 2D-focusing phased array with 512 antennas, 2 μm antenna pitch, 5 mm focal height, and 1550 nm wavelength. In the plane of the chip (Fig. 6.6e), the aperture is illuminated by the antennas. As the system scans to the expected focal plane 5 mm above the chip (Fig. 6.6d), the light is tightly-focused in both the x and y dimensions. At this height, a FWHM of ~6.4 μm is measured in the array dimension, x, closely matching the simulated value of 6.6 μm. Similarly, a FWHM of ~7.6 μm is measured in the antenna dimension, y, matching the expected value of 7.6 μm. Additionally, as expected, the angle in the antenna dimension is slightly offset. Finally, above the focal plane (Fig. 6.6c), the light is, once again, diffracted out. Note that, due to the favorable high enhancement of the focal spot, the light source inputted into the system had to be severely attenuated so that the IR camera did not artificially saturate at the focal plane while obtaining the data.

For comparison, a similar 1D-focusing array is also fabricated. The array utilizes the same splitter-tree architecture with 512 antennas, 2 μm antenna pitch, 5 mm focal height, and 1550 nm wavelength to focus in the array dimension; however, standard non-focusing antennas are used such that the system does not focus in the antenna

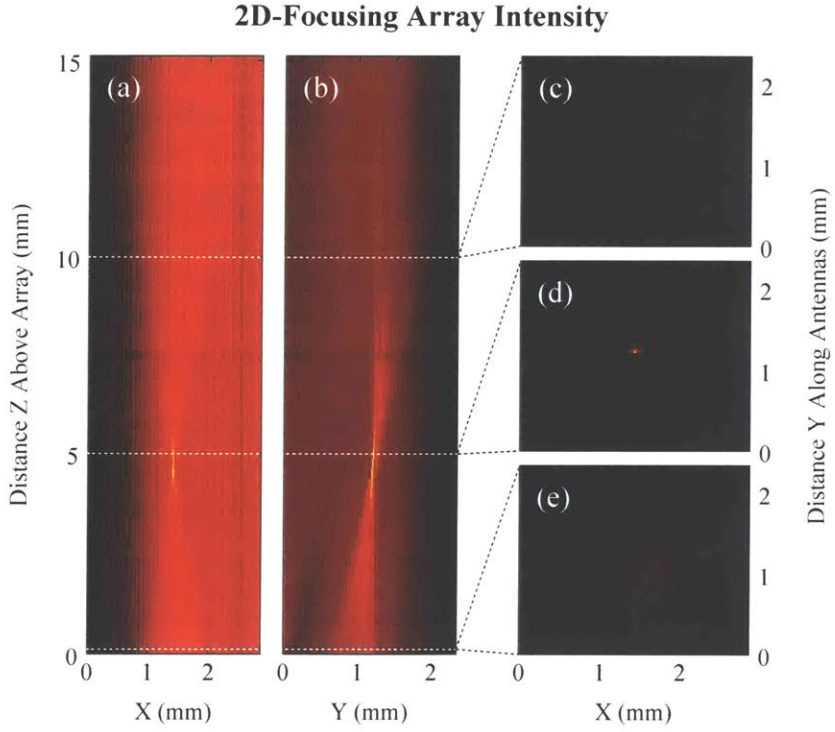

Figure 6.6: Measured cross-sectional intensity (in dB) above the chip for a 2D-focusing silicon splitter-tree-based phased array in the (a) x plane and (b) y plane with top-down intensity shown (e) in the plane of the chip, (d) at the focal plane, and (c) above the focal plane. Intensities are shown for an array with 512 antennas, 2 μm antenna pitch, 5 mm focal height, and 1550 nm wavelength.

dimension. The resulting cross-sectional intensity as a function of the distance above the chip and three top-down views are shown in Figs. 6.7a–d. In the plane of the chip (Fig. 6.7d), the aperture is illuminated by the antennas. As the system scans to the expected focal plane 5 mm above the chip (Fig. 6.7c), the light is tightly-focused in the array dimension to a FWHM of ~6.4μm which closely matches both the simulated and 2D-focusing results. Finally, above the focal plane (Fig. 6.7b), the light is, once again, diffracted out in the array dimension.

Similarly, both 1D- and 2D-focusing phased arrays are also fabricated with a 1 mm focal height. The resulting measured focal spots had FWHMs of ~1.7μm in the array dimension and ~2.9μm in the antenna dimension, compared to the simulated values of 1.4μm and 1.5μm, respectively. These slight discrepancies can be attributed to experimental error in measuring such small spot sizes with the finite IR-camera pixel

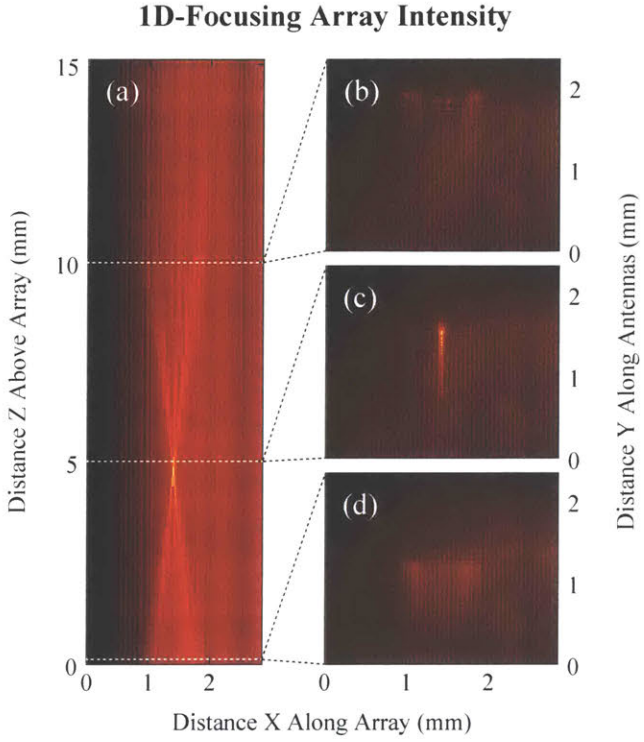

Figure 6.7: (a) Measured cross-sectional intensity (in dB) above the chip for a 1D-focusing silicon splitter-tree-based phased array with top-down intensity shown (d) in the plane of the chip, (c) at the focal plane, and (b) above the focal plane. Intensities are shown for an array with 512 antennas, 2 μm antenna pitch, 5 mm focal height, and 1550 nm wavelength.

size and compounding phase error in the antenna since the antenna is synthesized using the unwrapped phase which makes it more susceptible to phase variations.

6.3.3 Wavelength Steering in the Antenna Dimension

Finally, the wavelength of the light inputted into the 5-mm-focal-height 2D-focusing silicon array is swept to demonstrate wavelength steering in the antenna dimension. In theory, since the antennas are based on grating principals, as the wavelength of light is increased, the effective period of the antenna becomes smaller and the angle of the light radiated by the antenna varies such that the beam is offset closer to the input of the chip. Three cross-sectional intensities in the antenna dimension for wavelengths of 1550 nm, 1560 nm, and 1570 nm are shown in Fig. 6.8a–c. As expected,

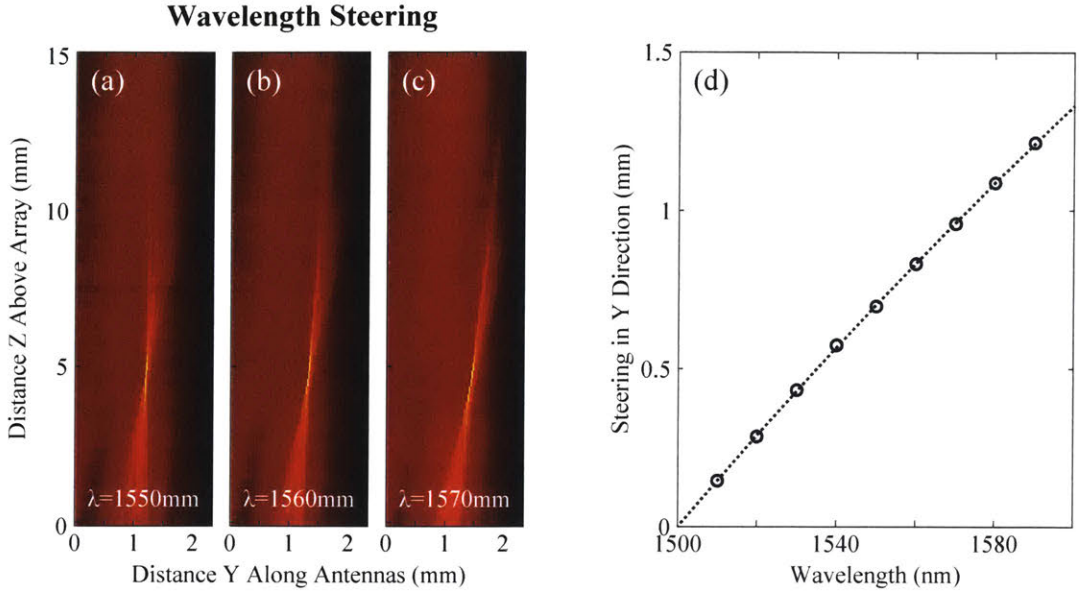

Figure 6.8: Measured cross-sectional intensity (in dB) above the chip for a 2D-focusing splitter-tree-based phased array at (a) 1550 nm, (b) 1560 nm, and (c) 1570 nm wavelengths. (d) Experimental results showing steering in the antenna dimension, y, versus wavelength. Results are shown for an array with 512 antennas, 2 μm antenna pitch, and 5 mm focal height.

as the wavelength is increased, the radiation angle is shifted while still maintaining its focusing characteristics. To quantify this shift, the offset of the beam in the antenna dimension is plotted as a function of the input wavelength as shown in Fig. 6.8d.

6.3.4 Discussion of Extension to Active Tuning and Future Work

Since the arrays are fabricated in a CMOS-compatible platform, they are naturally scalable to dynamic arbitrarily-tunable systems with active silicon-based phase shifters on each waveguide arm [67]. This extension of the system would enable steering of the focused spot in the array dimension in addition to the wavelength steering capability in the antenna dimension. However, although the array-dimension tuning would be fully arbitrary, this architecture is fundamentally limited to 2D-focusing in only one focal plane since the wavelength steering is only capable of inducing a lateral offset. For applications where both focal height and offset tuning is required,

a different architecture capable of scaling to electrical tuning in both dimensions is necessary.

In addition to this natural evolution to active systems, the demonstrations can be scaled to larger aperture sizes [23] to further reduce the focus spot size and enable larger focal heights. Additionally, to improve the field profile at the focal plane, the splitter-tree-based architecture can be modified to emit with a Gaussian amplitude profile by using a star coupler [27]. Finally, using similar synthesis algorithms as described in Sec. 4.7.3, the 2D-focusing arrays can be further improved by appropriately varying the perturbation strength of the focusing antennas in the array such that the antennas emit with either a uniform or Gaussian amplitude.

6.4 Focusing Pixel-Based Phased Arrays

Next, as a second method for experimentally demonstrating focusing integrated optical phased arrays, passive focusing phased arrays using the two-dimensional pixel-based architecture with the non-standard 380-nm height described in Ch. 5 are designed and fabricated as shown in Fig. 6.9. Specifically, focusing pixel-based arrays with 1024 antennas (i.e. 32 rows by 32 columns) and with 10,000 antennas (i.e. 100 rows by 100 columns) are demonstrated. By using the two-dimensional architecture and applying it to the focusing theory developed in Ch. 2, this system is capable of scaling to electrical phase control in both dimensions of the array to enable dynamic tuning of the spot's focal height and offset, simultaneously.

6.4.1 Implementation in the Pixel-Based Architecture

As described in Ch. 5, the pixel-based arrays consist of an input waveguide, a set of M row pixels which couple light from the input waveguide to M row waveguides, and a set of M emitter pixels on each row waveguide which couple light from each row waveguide into M antenna emitters to create an aperture of $M \times M$ antennas. In the following demonstrations, array sizes of $M = 32$ and $M = 100$ are chosen.

Within each row and emitter pixel, a directional coupler (see Sec. 5.2) is used for

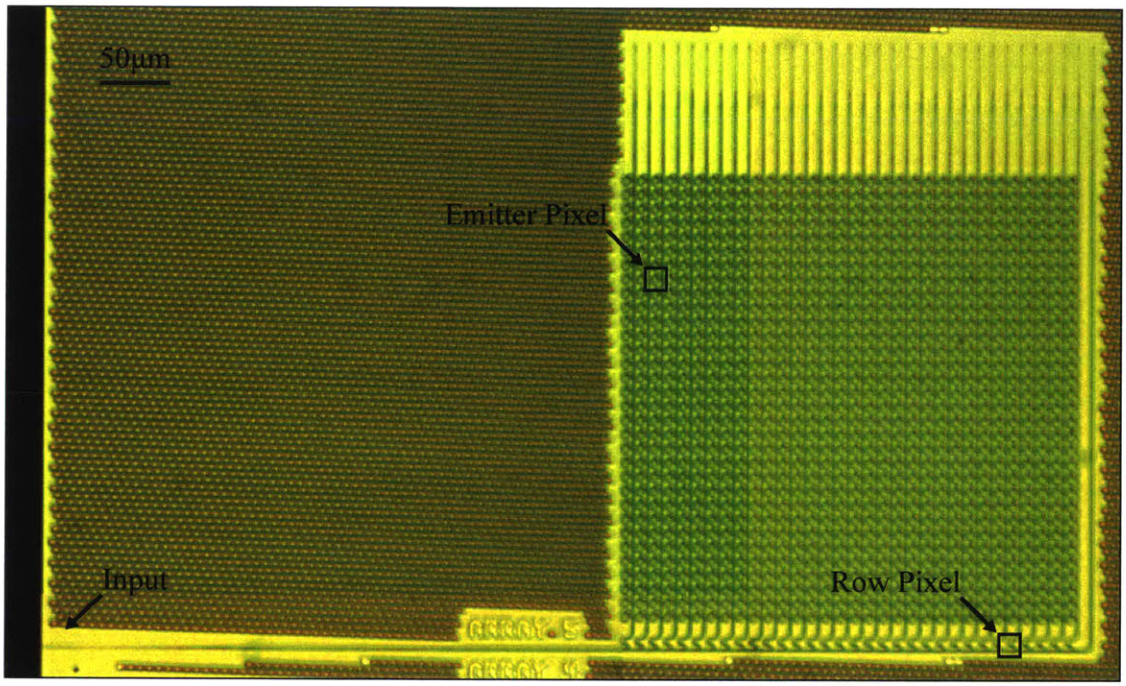

Figure 6.9: Micrograph of a fabricated two-dimensional pixel-based focusing phased array with 1024 antennas and 10 μm antenna pitch.

amplitude control. The coupling length and coupling gap of each directional coupler in the array are set such that the correct amplitude is feed into the emitters within the array. As shown in Sec. 2.1, to generate a focused beam using a phased array, a uniform element amplitude distribution can be used. As such, the power coupling coefficients for the directional couplers in the pixel-based array, given by Eqs. (5.1)–(5.2), can be simplified to

$$\eta_m = \frac{1}{M - m + N_{phantom} + 1} \tag{6.1}$$

where η_m is the coupling coefficient for both the m^{th} row pixel and the m^{th} emitter pixel within each row, M is the total number of rows and the total number of emitters in each row, m varies from 1 to M, and $N_{phantom}$ is the number of desired "phantom" antennas [31,70]. This phantom antenna concept is introduced to reduce the necessary coupling coefficient of the last pixel. Although this results in some power being discarded at the end of the input waveguide and each row waveguide, it eliminates

the need for the last direction coupler to have full 100% coupling which would require a relatively long coupling length and increase the pixel size [70]. For example, in this implementation, $N_{phantom}$ is set to 3 such that the highest coupling coefficient needed is 25%. Figure 6.10a shows the coupling lengths applied to each set of row or emitter pixels in an array with 1024 antennas, 10 μm antenna pitch, 5 mm focal height, and 1550 nm wavelength.

After each directional coupler, two compact adiabatic curves are placed and the offset length between them is varied to allow for arbitrary phase control to each row and emitter, as described in Sec. 5.3. However, since the phase required for focusing in two dimensions is separable, the phases for focusing in each dimension, given by Eq. (2.3), can be independently applied – i.e. the phase profile for focusing in the y dimension is applied to the coupler pixels while the phase profile for focusing in the x dimension is applied to the emitter pixels. Additionally, the phase encodings are modified to compensate for the variable phase induced by the direction couplers as discussed in in Sec. 5.3. Figure 6.10b shows the phase lengths applied to each set of row or emitter pixels in an array with 1024 antennas, 10 μm antenna pitch, 5 mm focal height, and 1550 nm wavelength.

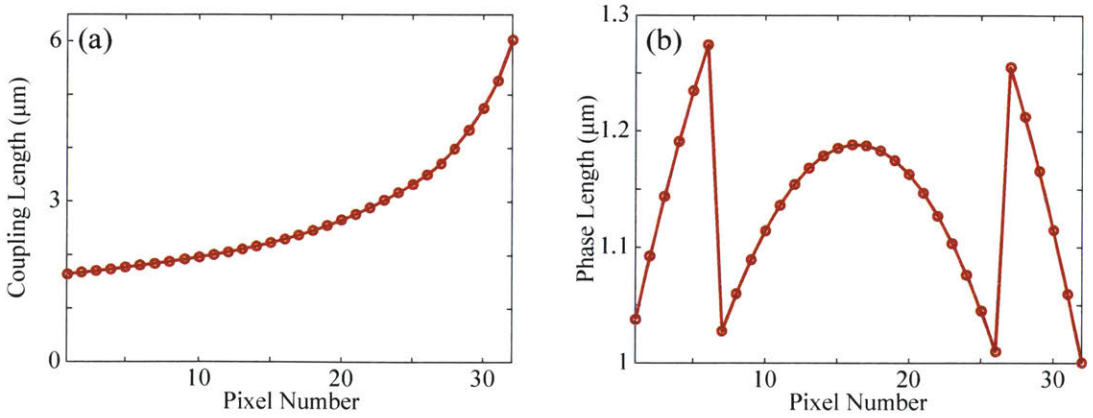

Figure 6.10: Synthesized (a) coupling waveguide lengths and (b) phase offset lengths versus pixel number for each set of row and emitter pixels for a focusing pixel-based phased array with 1024 antennas, 10 μm antenna pitch, 5 mm focal height, and 1550 nm wavelength.

6.4.2 Two-Dimensional-Focusing Experimental Results

The resulting cross-sectional intensity as a function of the distance above the chip and three top-down views are shown in Figs. 6.11a–e for the fabricated pixel-based 2D-focusing phased array with 1024 antennas (i.e. 32 rows by 32 columns), 10 μm antenna pitch, 5 mm focal height, and 1550 nm wavelength. Due to the 10 μm antenna pitch, multiple grating lobes are generated in the array factor in both the x and y dimensions. Two of these orders – the main beam and one of the second-order grating lobes – are seen in the camera's field of view in the x dimension as shown in Fig. 6.11a. As the system scans to the focal plane 5 mm above the chip (Fig. 6.11d), the main beam is tightly focused as expected. At this height, FWHMs of ~21.5μm are measured in both the x and y dimensions, closely matching the simulated value

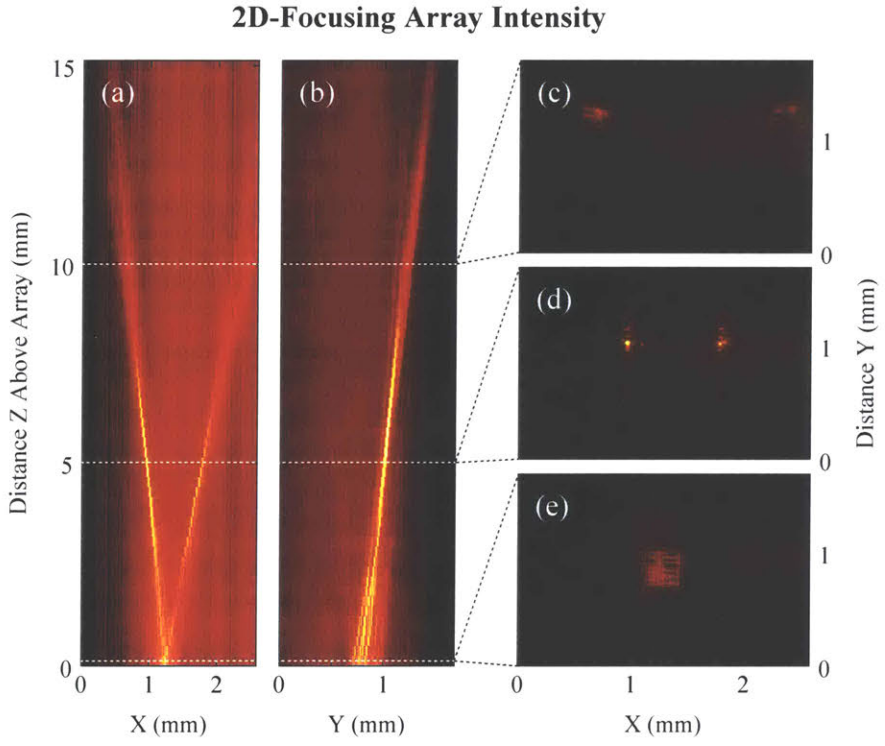

Figure 6.11: Measured cross-sectional intensity (in dB) above the chip for a 5 mm-focal-height pixel-based phased array in the (a) x plane and (b) y plane with top-down intensity shown (e) in the plane of the chip, (d) at the focal plane, and (c) above the focal plane. Intensities are shown for an array with 1024 antennas, 10 μm antenna pitch, and 1550 nm wavelength.

of 21.4μm.

For comparison, two additional 1024-antenna pixel-based arrays are fabricated with 3 mm and 10 mm focal heights. The measured FWHMs for all three arrays are plotted in Fig. 6.12 against the theory developed in Sec. 2.2 showing excellent agreement. As expected, the FWHM increases linearly with the focal height of the array.

Finally, a similar pixel-based array with 10,000 antennas (i.e. 100 rows by 100 columns) is fabricated. Since the aperture size of the array is significantly larger compared to the 1024 antenna array (1 mm × 1 mm versus 0.32 mm × 0.32 mm), the range of possible focal heights is greatly increased due to the quadratic scaling of the near-field boundary compared to the aperture size and the expected FWHMs are much smaller due to the inverse relationship of the aperture size and the FWHM. As such, for the fabricated 10,000-antenna 10-mm-focal-height array, the measured FWHMs in the x and y dimensions are ~23.3μm and ~20.9μm, respectively. However, due to the large number of antennas in the array, it is harder to evenly distribute power to each pixel in the array since lower coupling coefficients and higher precision are needed. As such, these measured FWHMs are larger than the simulated value of 13.5μm. In future implementations, lower coupling coefficients and higher precision could be achieved by varying the coupling gap as proposed in [31, 70].

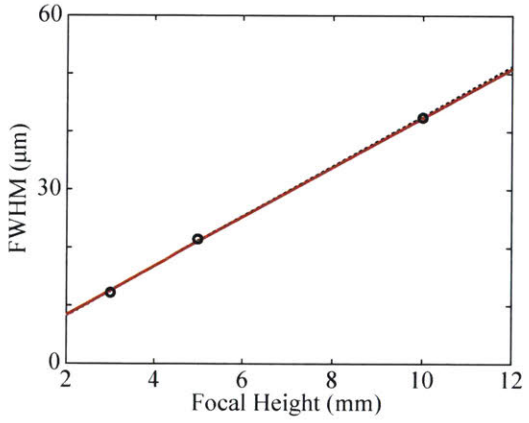

Figure 6.12: Simulated (red) and measured (black) power full-width half-maximum (FWHM) versus focal height. Results are shown for arrays with 1024 antennas, 10 μm antenna pitch, and 1550 nm wavelength.

6.4.3 Discussion of Extension to Active Tuning and Future Work

Similar to the splitter-tree-based architecture, since the pixel-based array is also fabricated in a CMOS-compatible platform, it is naturally scalable to a dynamic arbitrarily-tunable system with active silicon-based phase shifters integrated in each pixel as demonstrated in [25]. This extension of the system would enable both two-dimensional steering of the focused spot using the non-linear steering formulation developed in Sec. 2.3 and complete control of the focal height of the spot.

In addition to this natural evolution to active systems, the pixel-based architecture can be scaled to larger aperture sizes by engineer of the coupling gap to enable lower coupling coefficients and high precision [31, 70]. Additionally, to improve the field profile at the focal plane, the architecture can be modified to emit with a Gaussian amplitude profile by modifying the coupling coefficients of the array, as described in Sec. 7.2.1.

6.5 Conclusion

In summary, two architectures have been proposed for demonstrating passive focusing integrated optical phased arrays: a one-dimensional splitter-tree-based architecture with focusing antennas and a two-dimensional pixel-based architecture. Both architectures have been used to demonstrate a variety of aperture size and focal height arrays including a 512-antenna splitter-tree-based array with a $\sim$7 μm spot at a 5 mm focal height, a 1024-antenna pixel-based array with a $\sim$21 μm spot at a 5 mm focal height, and a 10,000-antenna pixel-based array with a $\sim$21 μm spot at a 10 mm focal height. The experimental results are summarized in Table 6.1.

Since the arrays are fabricated in CMOS-compatible platforms, they are naturally scalable to active arbitrarily-tunable systems with varying advantages. While the splitter-tree-based architecture is limited to active focusing in only one focal plane, it requires a smaller number of active controls and its close antenna pitch reduces the

Architecture	N	A	f_z	FWHM$_x$	FWHM$_y$
SiN Tree (1D)	128	0.5 mm × 1.2 mm	5 mm	~13μm	N/A
Si Tree (1D)	512	1.024 mm × 0.9 mm	1 mm	~1.7μm	N/A
Si Tree (2D)	512	1.024 mm × 0.9 mm	1 mm	~1.7μm	~2.9μm
Si Tree (1D)	512	1.024 mm × 0.9 mm	5 mm	~6.4μm	N/A
Si Tree (2D)	512	1.024 mm × 0.9 mm	5 mm	~6.4μm	~7.6μm
Pixel (2D)	1024	0.32 mm × 0.32 mm	3 mm	~12.2μm	~12.2μm
Pixel (2D)	1024	0.32 mm × 0.32 mm	5 mm	~21.5μm	~21.5μm
Pixel (2D)	1024	0.32 mm × 0.32 mm	10 mm	~45.9μm	~42.5μm
Pixel (2D)	10,000	1 mm × 1 mm	10 mm	~23.3μm	~20.9μm

Table 6.1: Summary of experimental results for various 1D- and 2D-focusing phased arrays showing array architecture (silicon-nitride splitter-tree-based 1D-focusing, silicon splitter-tree-based 1D-focusing, silicon splitter-tree-based 2D-focusing, or pixel-based 2D-focusing), number of antennas (N), aperture size (A), focal height (f_z), and FWHM in the x and y directions (FWHM$_x$ and FWHM$_y$, respectively).

number of grating lobes which increases the steering range of the device. In comparison, the pixel-based architecture enables control of the steering and focal height in both dimensions and could be arbitrary tuned without the need for a wavelength-tunable laser source; however, its large pixel pitch limits the steering range and it requires a larger number of active controls.

Chapter 7

Bessel-Beam Integrated Optical Phased Arrays

In this chapter, the splitter-tree-based and pixel-based phased array architectures are used to experimentally demonstrate quasi-Bessel-beam generating integrated optical phased arrays. First, the one-dimensional silicon-nitride splitter-tree-based architecture is implemented to demonstrate a 64-antenna integrated phased array with a 0.64 mm $\times$ 0.65 mm aperture which generates a Bessel-Gauss beam in the array axis with a $\sim$14 mm Bessel length and $\sim$30μm central-beam FWHM. Additionally, a gold wire is used to obstruct the radiated beam and demonstrate reforming of the central beam with its characteristic elongated profile. Next, the two-dimensional pixel-based architecture is utilized to show a second type of quasi-Bessel-beam-generating phased array with capabilities for generating fully-circularly-symmetric Bessel-Gauss beams. As a proof of concept, a 1024-antenna pixel-based variant with 32 rows by 32 columns and a 0.32 mm $\times$ 0.32 mm aperture is utilized to demonstrate Bessel-Gauss-beam formation in two-dimensions with a $\sim$30μm central-beam FWHM.

7.1 Quasi-Bessel-Beam Splitter-Tree-Based Phased Arrays

As a proof of concept, a passive quasi-1D Bessel-Gauss-beam-generating integrated optical phased array is designed and fabricated as shown in Fig. 7.1. The array transmits a Bessel-Gauss beam in the array axis and an exponentially decaying beam in the antenna axis (generation of quasi-one-dimensional Bessel beams has been explored [51]). The silicon-nitride one-dimensional splitter-tree-based phased array architecture, as developed in Ch. 4, is utilized in the demonstration.

7.1.1 Implementation in the Splitter-Tree-Based Architecture

The fabricated quasi-Bessel-beam-generating phased array utilizes the silicon-nitride splitter-tree-based architecture as developed in Ch. 4. A 6-layer multi-mode interference (MMI) splitter tree (see Sec. 4.4) is used to evenly distribute the input power to 64 waveguide arms with a final pitch of 10 μm. On each arm, a tap coupler structure (see Sec. 4.5) is placed to to couple a percentage of the light from each waveguide arm to a tap port while the remainder of the light in the thru port is routed off the chip. The length and coupling gap of each tap coupler in the array is chosen to enable a Gaussian feeding amplitude, given by Eq. (3.1), to the antennas as shown in Figs. 7.2a–b. On the output tap port of each coupler device, a phase taper structure (see Sec. 4.6.1) is placed which imparts a static phase delay dependent on the length

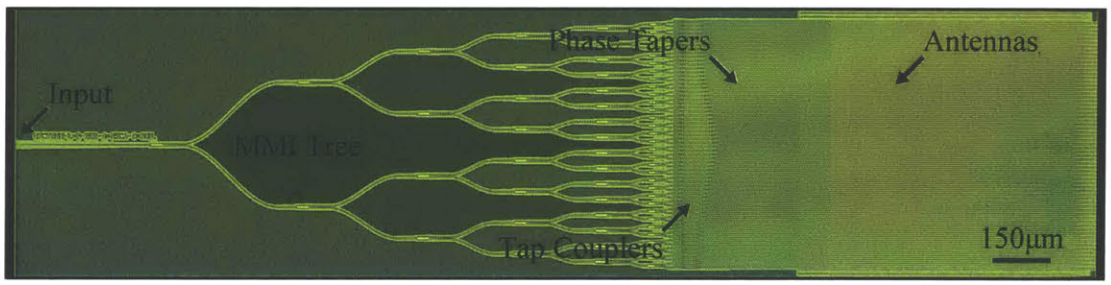

Figure 7.1: Micrograph of the fabricated splitter-tree-based quasi-Bessel-beam-generating phased array with 64 antennas and 10 μm antenna pitch.

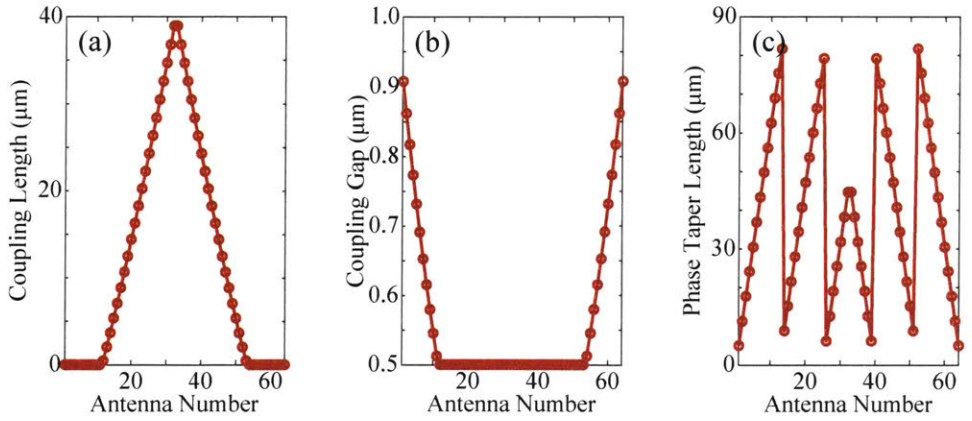

Figure 7.2: Synthesized (a) tap coupler length, (b) tap coupler gap, and (c) phase taper length versus antenna number for a quasi-Bessel-beam-generating splitter-tree-based phased array with 64 antennas, 10 μm antenna pitch, $\Phi_0 = 5\pi$, $A_0 = \sqrt{2}/2$, and 1550 nm wavelength.

of the device's wide section. By choosing the appropriate lengths for each taper as shown in Fig. 7.2c, the correct phase profile, given by Eq. (3.3), is applied. Finally, a 650-μm-long exponentially-radiating grating-based antenna (see Sec. 4.7.1) is placed on each arm to create a 0.64 mm × 0.65 mm aperture size.

7.1.2 One-Dimensional Quasi-Bessel-Beam Experimental Results

To characterize the array, the scanning optical imaging system developed in Sec. 6.1 is used. The resulting cross-sectional intensity as a function of the distance above the chip and three top-down views are shown in Figs. 7.3a–d for the fabricated quasi-Bessel-beam generating array with $\Phi_0 = 5\pi$ and $A_0 = \sqrt{2}/2$. In the plane of the chip (Fig. 7.3d), the aperture is illuminated by the antennas. As the system scans through the Bessel region of the beam (Fig. 7.3c), a characteristic one-dimensional Bessel-Gauss beam is observed with an elongated yet narrow central beam. In this region, a central-beam FWHM of ~30μm is measured along the Bessel length, closely matching the simulated value of 30.7μm. Finally, above the Bessel length (Fig. 7.3b), the central beam is destroyed, the Bessel breaks down, and the light begins diffracting outwards. The measured Bessel length of ~14 mm is slightly longer than the simulated

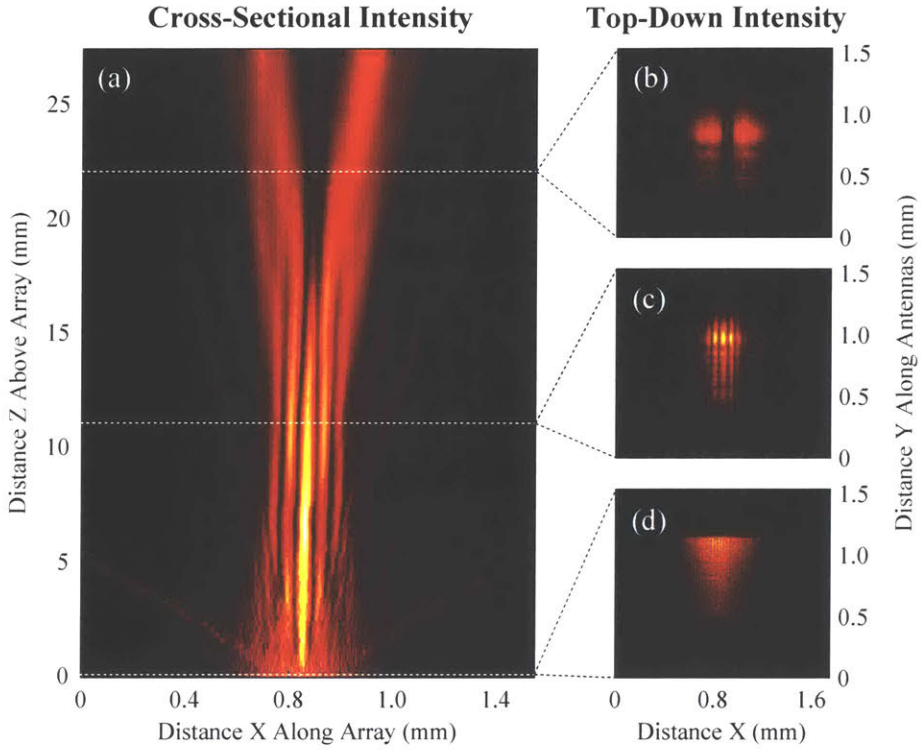

Figure 7.3: (a) Measured cross-sectional intensity (in dB) above the chip for a quasi-Bessel-beam-generating phased array with top-down intensity shown (d) in the plane of the chip ($z = 0\,\text{mm}$), (c) within the Bessel region of the emitted beam ($z = 11\,\text{mm}$), and (b) after breakdown of the Bessel region ($z = 22\,\text{mm}$). Intensities are shown for an array with 64 antennas, 10 μm antenna pitch, $\Phi_0 = 5\pi$, $A_0 = \sqrt{2}/2$, and 1550 nm wavelength.

value of 11.4 mm. This deviation can be attributed to the imperfect performance of the tap couplers (as shown in Sec. 4.5) which deforms the feeding amplitude profile of the device.

Next, an 18-μm-diameter gold wire is placed in the path of the central beam along the antenna axis 7.5 mm above the chip. The resulting cross-sectional intensity as a function of the distance above the chip and three top-down views are shown in Figs. 7.4a–d. As shown in Fig. 7.4d, the wire obstructs the central beam. However, the central beam reforms after a shadow-zone length and continues to propagate with its characteristic elongated profile even after obstruction as shown in Fig. 7.4b.

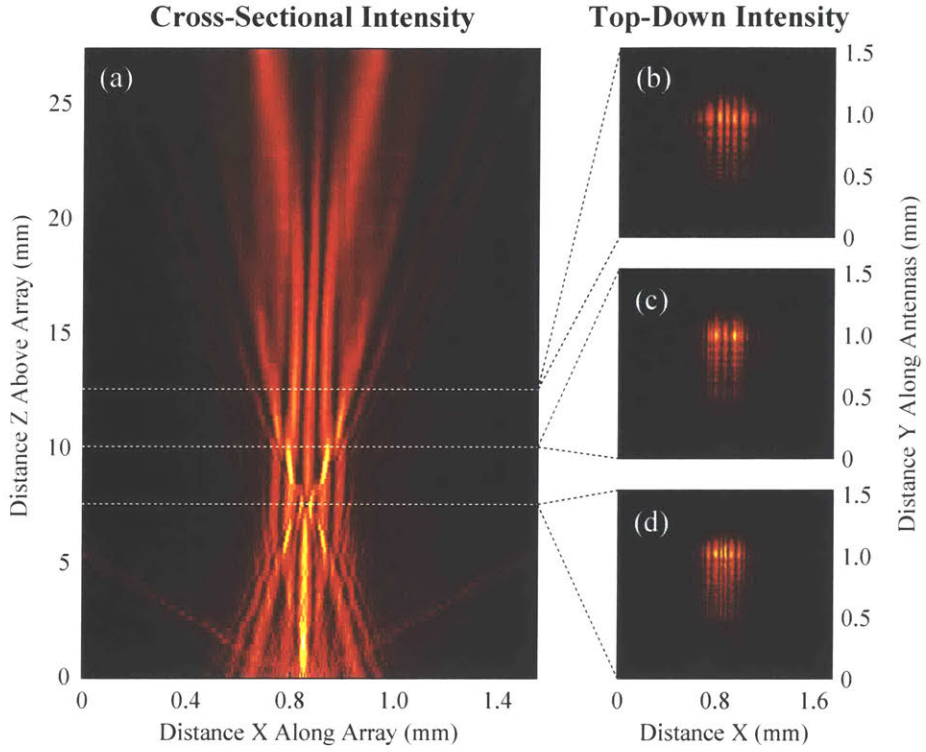

Figure 7.4: (a) Measured cross-sectional intensity (in dB) above the chip for a quasi-Bessel beam generated by a phased array when obstructed by a gold wire. Top-down intensities are shown (d) in the plane of the obstacle ($z = 7.5\,\text{mm}$), (c) within the shadow zone of the obstacle ($z = 10\,\text{mm}$), and (b) after reformation of the central beam ($z = 12.5\,\text{mm}$). Intensities are shown for an array with 64 antennas, $10\,\mu\text{m}$ antenna pitch, $\Phi_0 = 5\pi$, $A_0 = \sqrt{2}/2$, and 1550 nm wavelength.

7.1.3 Discussion of Future Work

Since the array is fabricated in a CMOS-compatible platform, it is naturally scalable to an active arbitrarily-tunable fully-integrated system through interfacing with active silicon-based phase shifters [67]. Additionally, two-dimensional Bessel-Gauss-beam generation can be achieved in this architecture by appropriately shaping the phase and amplitude characteristics of the antennas in the splitter-tree-based array through apodization of the period and perturbation strength along the antenna [61] similar to the synthesis technique developed in Sec. 4.7.3. Furthermore, the loss naturally induced by the tap coupler amplitude approach in the array can be eliminated by using a star coupler which simultaneously splits the signal and imparts a Gaussian amplitude profile [27]. Finally, the demonstration can be scaled to larger

aperture sizes to enable longer Bessel lengths; for example, assuming the 4 mm aperture previously demonstrated in this platform [23], a 0.48 m Bessel length could be demonstrated.

7.2 Quasi-Bessel-Beam Pixel-Based Phased Arrays

Next, as a second method for generating quasi-Bessel-beams using integrated optical phased arrays, a passive quasi-Bessel-beam-generating phased array using the two-dimensional pixel-based architecture with the standard 220-nm height described in Ch. 5 is synthesized and fabricated. Specifically, a quasi-Bessel-beam-generating pixel-based array with 1024 antennas (i.e. 32 rows by 32 columns) is demonstrated. By using the two-dimensional architecture and applying it to the Bessel theory developed in Ch. 3, the array generates a Bessel-Gauss beam in two dimensions with future capabilities for generating a fully-circularly-symmetric Bessel-Gauss beam.

7.2.1 Implementation in the Pixel-Based Architecture

As described in Ch. 5, the pixel-based arrays consist of an input waveguide, a set of M row pixels which couple light from the input waveguide to M row waveguides, and a set of M emitter pixels on each row waveguide which couple light from each row waveguide into M antenna emitters to create an aperture of $M \times M$ antennas. In the following implementation, an array with $M = 32$ is demonstrated.

Within each row and emitter pixel, a directional coupler (see Sec. 5.2) is used for amplitude control. The coupling length and coupling gap of each directional coupler in the array are set such that the correct amplitude is feed into the emitters within the array. As shown in Sec. 3.2, to generate a Bessel-Gauss beam using a phased array, a Gaussian element amplitude distribution must be used. Since the desired Gaussian distribution is separable, the required power coupling coefficients for the row pixels and emitter pixels are the same. As such, the coefficients for all sets of directional

couplers, given by Eqs. (5.1)–(5.2), can be simplified to

$$\eta_m = \frac{A_m^2}{A_M^2 + \sum_{j=m}^{M} A_j^2} \tag{7.1}$$

where η_m is the coupling coefficient for both the m^{th} row pixel and the m^{th} emitter pixel within each row, M is the total number of rows and the total number of emitters in each row, m varies from 1 to M, and A_m is given by Eq. (3.1). Figure 7.5a shows the coupling lengths applied to each set of row or emitter pixels in an array with 1024 antennas, $A_0 = \sqrt{2\ln 2}/2$ amplitude parameter, and 1550 nm wavelength.

After each directional coupler, two compact adiabatic curves are placed and the offset length between them is varied to allow for arbitrary phase control to each row and emitter, as described in Sec. 5.3. In this implementation, the Axion phase profile necessary for Bessel-Gauss-beam generation, given by Eq. (3.3), is independently applied to the row pixels and the emitter pixels such that a Bessel-Gauss beam is generated in the x and in the y dimension. Additionally, the phase encodings are modified to compensate for the variable phase induced by the direction couplers as discussed in in Sec. 5.3.2. Figure 7.5b shows the phase lengths applied to each set of row or emitter pixels in an array with 1024 antennas, $\Phi_0 = 3\pi$ phase parameter, and

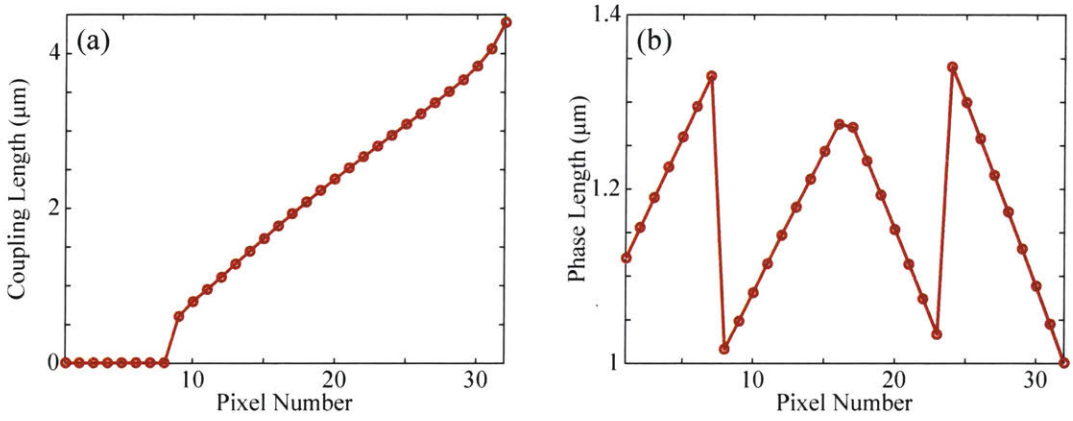

Figure 7.5: Synthesized (a) coupling waveguide lengths and (b) phase offset lengths versus pixel number for each set of row and emitter pixels for a quasi-Bessel-beam-generating pixel-based phased array with 1024 antennas, 10 μm antenna pitch, $\Phi_0 = 3\pi$, $A_0 = \sqrt{2\ln 2}/2$, and 1550 nm wavelength.

1550 nm wavelength.

7.2.2 Two-Dimensional Quasi-Bessel-Beam Experimental Results

The resulting intensity above the chip for the quasi-Bessel-beam-generating pixel-based array with 1024 antennas, 10 μm antenna pitch, $\Phi_0 = 3\pi$, $A_0 = \sqrt{2\ln 2}/2$, and 1550 nm wavelength is shown in Fig. 7.6. Due to the 10 μm antenna pitch, multiple grating lobes are generated in the array factor in both the x and y dimensions. Two of these orders – the main beam and one of the second-order grating lobes – are clearly seen in the camera's field of view in the x dimension and two additional orders are faintly seen in the y dimension. As expected, within the Bessel region, the array generates a Bessel-Gauss beam in the x and y dimensions within each grating lobe. A central-beam main-lobe FWHM of ~36μm and ~27μm is measured in the x and

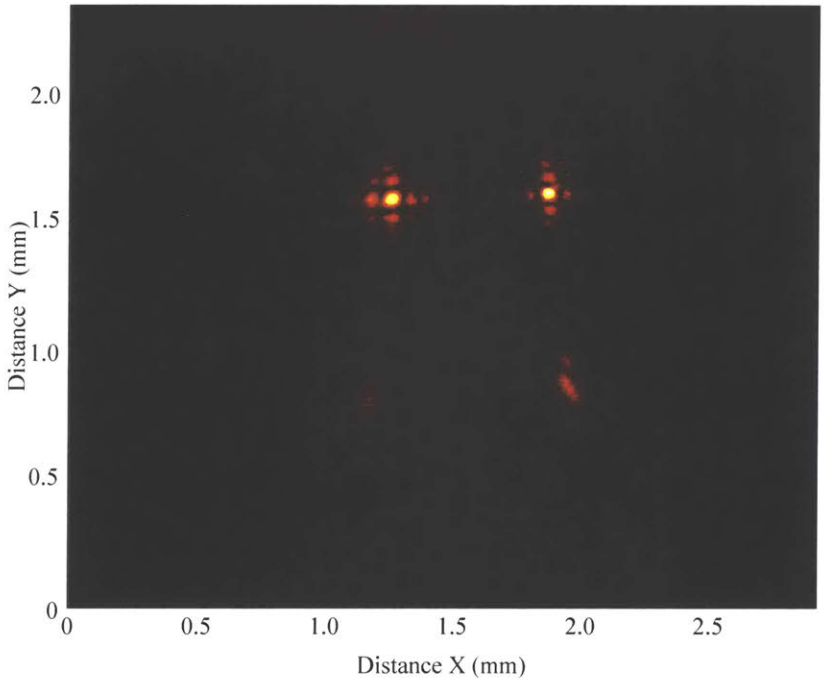

Figure 7.6: Measured top-down intensity (in dB) above the chip within the Bessel region for a quasi-Bessel-beam-generating pixel-based phased array. Intensity is shown for an array with 1024 antennas, 10 μm antenna pitch, $\Phi_0 = 3\pi$, $A_0 = \sqrt{2\ln 2}/2$, and 1550 nm wavelength.

y dimensions, respectively, closely matching the simulated value of 28.2μm.

7.2.3 Discussion of Future Work

The pixel-based architecture can be further utilized to generate a fully-circularly-symmetric Bessel-Gauss beam. In order to generate a full Bessel-Gauss beam, instead of applying the appropriate phase encoding independently to the row and emitter pixels, the entire phase profile must be generated using a two-dimensional mapping. Figure 7.7 shows the compounded effect of applying the "Axicon" phase independently on the row and emitter pixels versus the proposed direct two-dimensional mapping. As shown, the two-dimensional mapping could be used to more accurate mimic an Axicon lens to enable circularly-symmetric Bessel-Gauss-beam generation.

Additionally, since the array is fabricated in a CMOS-compatible platform, it is naturally scalable to an active arbitrarily-tunable fully-integrated system through interfacing with active silicon-based phase shifters within each row and emitter pixel [25,67]. Finally, the demonstration can be scaled to larger aperture sizes, such as the 10,000 array demonstrated in Sec. 6.4, to enable longer Bessel lengths.

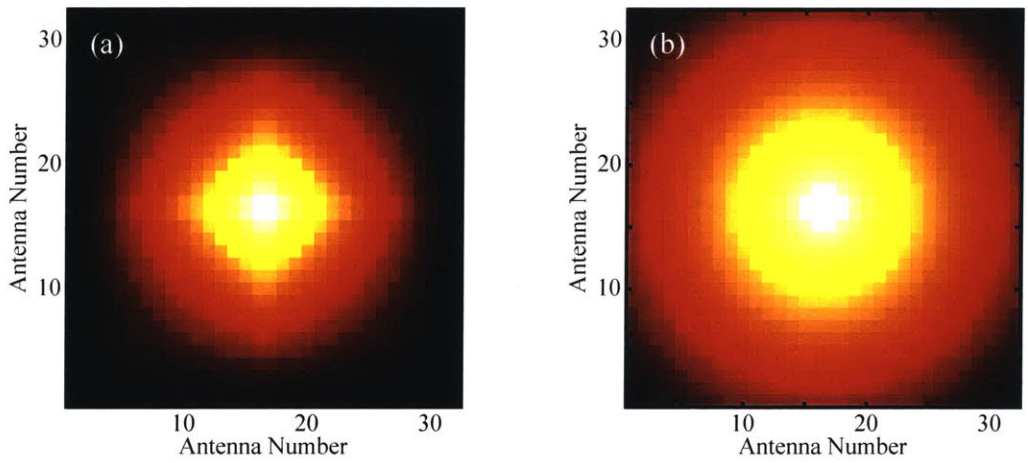

Figure 7.7: Phase encoding for a two-dimensional pixel-based quasi-Bessel-beam-generating array with 1024 antennas showing (a) the compounding effect of applying the Axicon phase independently on the row and emitter pixels versus (b) directly applying a two-dimensional Axicon mapping. Phases are shown without 2π phase wrapping.

7.3 Conclusion

In summary, this chapter presents the first proposal and demonstration of integrated optical phased arrays which generate quasi-Bessel beams in the near field of the array. The splitter-tree-based architecture has been utilized to demonstrate a quasi-one-dimensional Bessel-Gauss-beam-generating phased array which transmits a Bessel-Gauss-beam in one dimension with a $\sim$14 mm Bessel length and $\sim$30μm central-beam FWHM. Next, the pixel-based phased array architecture has been implemented to generate a Bessel-Gauss-beam in two dimensions with a measured FWHM of $\sim$30μm and a two-dimensional phase encoding has been presented for application of the system to demonstrate a fully-circularly-symmetric Bessel-Gauss-beam.

Chapter 8

Conclusion

8.1 Summary of Thesis

In summary, in this work, a variety of integrated optical phased arrays with capabilities for applications in optical trapping have been proposed, developed, and experimentally demonstrated. Specifically, integrated optical phased arrays which focus radiated light to tightly-confined spots in the near field have been demonstrated for the first time. Additionally, this work has presented the first proposal and demonstration of integrated optical phased arrays which generate quasi-Bessel beams in the near field of the array.

To enable these demonstrations, relevant theory for focusing and Bessel-beam phased arrays has been developed and discussed. Foremost, the phase profiles necessary for generating focusing beams with non-linear steering using phased arrays have been derived, and the effects of the aperture size and focal height on the full-width half-maximum (FWHM) have been simulated and discussed. Furthermore, the phases and amplitudes necessary for Bessel-Gauss beam generation have been developed, and relevant variables and parameters – including the aperture size, maximum phase variation, Gaussian FWHM parameter, Bessel length, and central-beam FWHM – have been presented and discussed.

Additionally, two architectures have been proposed for demonstrating passive near-field focusing and quasi-Bessel-beam-generating integrated optical phased ar-

rays. First, a one-dimensional splitter-tree-based phased array architecture has been modified to passively encode arbitrary phase and amplitude distributions to the elements of the array – necessary for focused and Bessel-Gauss-beam generation. Although this architecture is capable of wavelength steering in the antenna dimension, it is limited to arbitrary electronic control in only the array dimension. As such, a two-dimensional pixel-based architecture has also been utilized to show a second type of focusing and Bessel-Gauss-generating passive phased array with capabilities for active electronic control in two dimensions. To enable these phased array systems, a suite of integrated nanophotonic devices for waveguiding, coupling, routing, phase control, and radiation have been developed, numerically simulated, fabricated, and experimentally demonstrated.

Using the developed theory and architectures, a variety of focusing and Bessel-beam integrated optical phased arrays have been experimentally demonstrated. First, both architectures have been used to demonstrate a variety of aperture size and focal height focusing arrays, including a 512-antenna splitter-tree-based array with a $\sim$7 μm spot at a 5 mm focal height, a 1024-antenna pixel-based array with a $\sim$21 μm spot at a 5 mm focal height, and a 10,000-antenna pixel-based array with a $\sim$21 μm spot at a 10 mm focal height. Next, the splitter-tree-based architecture has been utilized to demonstrate a quasi-one-dimensional Bessel-Gauss-beam-generating phased array which transmits a Bessel-Gauss-beam in one dimension with a $\sim$14 mm Bessel length and $\sim$30 μm central-beam FWHM, and the pixel-based phased array architecture has been implemented to generate a Bessel-Gauss-beam in two dimensions with a measured central-beam FWHM of $\sim$30μm. Additionally, discussion on scaling of the various architectures and arrays to active arbitrarily-tunable systems and future improvements of the systems have been presented.

8.2 Optical Trapping and Additional Applications

The demonstrated on-chip focusing and Bessel-beam optical phased arrays provide one possible approach to scaling and arbitrary tweezing of optical traps. For example,

by enabling highly-enhanced tightly-focused beams with large focal heights, the focusing systems open up new possibilities for large-scale biological characterization and monitoring through optical trapping [4–7], especially for *en vivo* experiments wherein relatively large offsets are an advantage [5]. Similarly, leveraging the elongated properties of Bessel-Gauss beams, the quasi-Bessel-beam-generating phased arrays could enable chip-based multi-particle trapping in multiple spatially-separated planes [42].

Furthermore, the demonstrated focusing and Bessel-beam integrated optical phased arrays have important applications in a variety of additional areas. For example, by enabling a chip-based source of highly-focused beams, the focusing systems have applications in chip-scale laser lithography techniques ranging from trapping-based nano-assembly [8, 9] to selective laser melting additive manufacturing [74]. Furthermore, by generating quasi-Bessel beams in a fully-integrated, compact form-factor system, the Bessel-beam phased arrays promise new developments in scalable and adaptive optical communications [48] and microscopy [43, 44].

8.3 Acknowledgments

The author thanks Professor Michael Watts for the opportunity to develop and work on this project, for providing the financial and logistical resources without which this work would not have been possible, and for his mentorship, genuine feedback, and overall support.

Additionally, the author thanks all members, past and present, of the Photonic Microsystems Group for insightful discussions, for establishment of the group's simulation, layout, and experimental infrastructure, and for development of the silicon photonics platform. Special thanks is given to Christopher V. Poulton, Matthew J. Byrd, and Manan Raval for all of the fruitful discussions, for their exceptional design work and silicon photonics expertise, and for the immeasurable general assistance they provided which were vital for this work.

The devices demonstrated throughout this work were fabricated at the Colleges of Nanoscale Science and Engineering (CNSE) at the SUNY Polytechnic Institute in

Albany, New York, under the supervision of Douglas D. Coolbaugh, Daniel Coleman, Nicholas M. Fahrenkopf, and Christopher Baiocco.

This work was supported by the Defense Advanced Research Projects Agency (DARPA) Electronic-Photonic Heterogeneous Integration (E-PHI) program (Grant No. HR0011-12-2-0007), the National Science Foundation (NSF) Graduate Research Fellowship Program (GRFP) (Grant No. 1122374), and a Massachusetts Institute of Technology Grier Presidential Fellowship.

Bibliography

[1] A. Ashkin, J. Dziedzic, J. Bjorkholm, and S. Chu, "Observation of a single-beam gradient force optical trap for dielectric particles," *Optics letters*, vol. 11, no. 5, pp. 288–290, 1986.

[2] D. G. Grier, "A revolution in optical manipulation," *Nature*, vol. 424, no. 6950, pp. 810–816, 2003.

[3] C. Xie, C. Goodman, M. A. Dinno, and Y.-Q. Li, "Real-time raman spectroscopy of optically trapped living cells and organelles," *Optics Express*, vol. 12, no. 25, pp. 6208–6214, 2004.

[4] C. Bustamante, Z. Bryant, and S. B. Smith, "Ten years of tension: single-molecule dna mechanics," *Nature*, vol. 421, no. 6921, pp. 423–427, 2003.

[5] M.-C. Zhong, X.-B. Wei, J.-H. Zhou, Z.-Q. Wang, and Y.-M. Li, "Trapping red blood cells in living animals using optical tweezers," *Nature communications*, vol. 4, p. 1768, 2013.

[6] B. Akiyoshi, K. K. Sarangapani, A. F. Powers, C. R. Nelson, S. L. Reichow, H. Arellano-Santoyo, T. Gonen, J. A. Ranish, C. L. Asbury, and S. Biggins, "Tension directly stabilizes reconstituted kinetochore-microtubule attachments," *Nature*, vol. 468, no. 7323, pp. 576–579, 2010.

[7] G. Popescu, K. Park, M. Mir, and R. Bashir, "New technologies for measuring single cell mass," *Lab on a Chip*, vol. 14, no. 4, pp. 646–652, 2014.

[8] P. J. Pauzauskie, A. Radenovic, E. Trepagnier, H. Shroff, P. Yang, and J. Liphardt, "Optical trapping and integration of semiconductor nanowire assemblies in water," *Nature materials*, vol. 5, no. 2, pp. 97–101, 2006.

[9] S. H. Simpson and S. Hanna, "Holographic optical trapping of microrods and nanowires," *JOSA A*, vol. 27, no. 6, pp. 1255–1264, 2010.

[10] D. Barredo, S. de Léséleuc, V. Lienhard, T. Lahaye, and A. Browaeys, "An atom-by-atom assembler of defect-free arbitrary two-dimensional atomic arrays," *Science*, vol. 354, no. 6315, pp. 1021–1023, 2016.

[11] M. Endres, H. Bernien, A. Keesling, H. Levine, E. R. Anschuetz, A. Krajenbrink, C. Senko, V. Vuletic, M. Greiner, and M. D. Lukin, "Atom-by-atom assembly of defect-free one-dimensional cold atom arrays," *Science*, p. aah3752, 2016.

[12] P. Jing, J. Wu, G. W. Liu, E. G. Keeler, S. H. Pun, and L. Y. Lin, "Photonic crystal optical tweezers with high efficiency for live biological samples and viability characterization," *Scientific reports*, vol. 6, 2016.

[13] C. Renaut, B. Cluzel, J. Dellinger, L. Lalouat, E. Picard, D. Peyrade, E. Hadji, and F. De Fornel, "On chip shapeable optical tweezers," *Scientific reports*, vol. 3, 2013.

[14] S. Mandal, X. Serey, and D. Erickson, "Nanomanipulation using silicon photonic crystal resonators," *Nano letters*, vol. 10, no. 1, pp. 99–104, 2009.

[15] C. Renaut, J. Dellinger, B. Cluzel, T. Honegger, D. Peyrade, E. Picard, F. De Fornel, and E. Hadji, "Assembly of microparticles by optical trapping with a photonic crystal nanocavity," *Applied Physics Letters*, vol. 100, no. 10, p. 101103, 2012.

[16] Y.-F. Chen, X. Serey, R. Sarkar, P. Chen, and D. Erickson, "Controlled photonic manipulation of proteins and other nanomaterials," *Nano letters*, vol. 12, no. 3, p. 1633, 2012.

[17] G. Magno, A. Ecarnot, C. Pin, V. Yam, P. Gogol, R. Mégy, B. Cluzel, and B. Dagens, "Integrated plasmonic nanotweezers for nanoparticle manipulation," *Optics Letters*, vol. 41, no. 16, pp. 3679–3682, 2016.

[18] M. L. Juan, M. Righini, and R. Quidant, "Plasmon nano-optical tweezers," *Nature Photonics*, vol. 5, no. 6, pp. 349–356, 2011.

[19] L. Huang, S. J. Maerkl, and O. J. Martin, "Integration of plasmonic trapping in a microfluidic environment," *Optics express*, vol. 17, no. 8, pp. 6018–6024, 2009.

[20] H. Wong, M. Righini, J. Gates, P. Smith, V. Pruneri, and R. Quidant, "On-a-chip surface plasmon tweezers," *Applied Physics Letters*, vol. 99, no. 6, p. 061107, 2011.

[21] S. Lin and K. B. Crozier, "Planar silicon microrings as wavelength-multiplexed optical traps for storing and sensing particles," *Lab on a Chip*, vol. 11, no. 23, pp. 4047–4051, 2011.

[22] H. Cai and A. W. Poon, "Optical manipulation and transport of microparticles on silicon nitride microring-resonator-based add–drop devices," *Optics letters*, vol. 35, no. 17, pp. 2855–2857, 2010.

[23] C. V. Poulton, M. J. Byrd, M. Raval, Z. Su, N. Li, E. Timurdogan, D. Coolbaugh, D. Vermeulen, and M. R. Watts, "Large-scale silicon nitride nanophotonic phased arrays at infrared and visible wavelengths," *Optics Letters*, vol. 42, no. 1, pp. 21–24, 2017.

[24] F. Aflatouni, B. Abiri, A. Rekhi, and A. Hajimiri, "Nanophotonic projection system," *Optics Express*, vol. 23, no. 16, pp. 21012–21022, 2015.

[25] J. Sun, E. Timurdogan, A. Yaacobi, E. S. Hosseini, and M. R. Watts, "Large-scale nanophotonic phased array," *Nature*, vol. 493, no. 7431, pp. 195–199, 2013.

[26] S. Chung, H. Abediasl, and H. Hashemi, "15.4 a 1024-element scalable optical phased array in 0.18 μm soi cmos," in *Solid-State Circuits Conference (ISSCC), 2017 IEEE International*, pp. 262–263, IEEE, 2017.

[27] D. N. Hutchison, J. Sun, J. K. Doylend, R. Kumar, J. Heck, W. Kim, C. T. Phare, A. Feshali, and H. Rong, "High-resolution aliasing-free optical beam steering," *Optica*, vol. 3, no. 8, pp. 887–890, 2016.

[28] T. Komljenovic, R. Helkey, L. Coldren, and J. E. Bowers, "Sparse aperiodic arrays for optical beam forming and lidar," *Optics Express*, vol. 25, no. 3, pp. 2511–2528, 2017.

[29] J. Sun, E. shah Hosseini, A. Yaacobi, D. B. Cole, G. Leake, D. Coolbaugh, and M. R. Watts, "Two-dimensional apodized silicon photonic phased arrays," *Optics letters*, vol. 39, no. 2, pp. 367–370, 2014.

[30] C. V. Poulton, A. Yaccobi, Z. Su, M. J. Byrd, and M. R. Watts, "Optical phased array with small spot size, high steering range and grouped cascaded phase shifters," in *Integrated Photonics Research, Silicon and Nanophotonics*, pp. IW1B–2, Optical Society of America, 2016.

[31] J. Zhou, J. Sun, A. Yaacobi, C. V. Poulton, and M. Watts, "Design of 3d hologram emitting optical phased arrays," in *Integrated Photonics Research, Silicon and Nanophotonics*, p. IT4A.7, Optical Society of America, 2015.

[32] J. Notaros, C. V. Poulton, M. Raval, M. J. Byrd, D. Coolbaugh, and M. R. Watts, "Fresnel-lens-inspired focusing phased arrays for optical trapping applications," in *CLEO: Science and Innovations*, p. STh1M.3, Optical Society of America, 2017.

[33] J. Notaros, C. V. Poulton, M. J. Byrd, M. Raval, and M. R. Watts, "Integrated optical phased arrays for quasi-bessel-beam generation." in preparation.

[34] J. Notaros, C. V. Poulton, M. Raval, and M. R. Watts, "Near-field focusing integrated optical phased arrays for optical trapping applications." in preparation.

[35] C. V. Poulton, "Integrated lidar with optical phased arrays in silicon photonics," Master's thesis, Massachusetts Institute of Technology, 2016.

[36] B. Notaros, *Electromagnetics.* Prentice Hall, 2011.

[37] J. Durnin, "Exact solutions for nondiffracting beams. i. the scalar theory," *JOSA A*, vol. 4, no. 4, pp. 651–654, 1987.

[38] F. Gori, G. Guattari, and C. Padovani, "Bessel-gauss beams," *Optics Communications*, vol. 64, no. 6, pp. 491–495, 1987.

[39] Z. Bouchal, J. Wagner, and M. Chlup, "Self-reconstruction of a distorted nondiffracting beam," *Optics Communications*, vol. 151, no. 4, pp. 207–211, 1998.

[40] J. Chen, J. Ng, Z. Lin, and C. Chan, "Optical pulling force," *Nature Photonics*, vol. 5, no. 9, pp. 531–534, 2011.

[41] D. McGloin and K. Dholakia, "Bessel beams: diffraction in a new light," *Contemporary Physics*, vol. 46, no. 1, pp. 15–28, 2005.

[42] V. Garces-Chavez, D. McGloin, H. Melville, W. Sibbett, and K. Dholakia, "Simultaneous micromanipulation in multiple planes using a self-reconstructing light beam," *Nature*, vol. 419, no. 6903, pp. 145–147, 2002.

[43] F. O. Fahrbach, P. Simon, and A. Rohrbach, "Microscopy with self-reconstructing beams," *Nature Photonics*, vol. 4, no. 11, pp. 780–785, 2010.

[44] P. Dufour, M. Piché, Y. De Koninck, and N. McCarthy, "Two-photon excitation fluorescence microscopy with a high depth of field using an axicon," *Applied Optics*, vol. 45, no. 36, pp. 9246–9252, 2006.

[45] L. Yang, S. Ji, K. Xie, W. Du, B. Liu, Y. Hu, J. Li, G. Zhao, D. Wu, W. Huang, S. Liu, H. Jiang, and J. Chu, "High efficiency fabrication of complex microtube arrays by scanning focused femtosecond laser bessel beam for trapping/releasing biological cells," *Optics Express*, vol. 25, no. 7, pp. 8144–8157, 2017.

[46] D. Li, K. Imasaki, S. Miyamoto, S. Amano, and T. Mochizuki, "Conceptual design of bessel beam cavity for free-electron laser," *International Journal of Infrared and Millimeter Waves*, vol. 27, no. 2, pp. 165–171, 2006.

[47] O. Ren and R. Birngruber, "Axicon: a new laser beam delivery system for corneal surgery," *IEEE Journal of Quantum Electronics*, vol. 26, no. 12, pp. 2305–2308, 1990.

[48] S. Li and J. Wang, "Adaptive free-space optical communications through turbulence using self-healing bessel beams," *Scientific Reports*, vol. 7, 2017.

[49] N. Chattrapiban, E. A. Rogers, D. Cofield, W. T. Hill III, and R. Roy, "Generation of nondiffracting bessel beams by use of a spatial light modulator," *Optics Letters*, vol. 28, no. 22, pp. 2183–2185, 2003.

[50] P. García-Martínez, M. M. Sánchez-López, J. A. Davis, D. M. Cottrell, D. Sand, and I. Moreno, "Generation of bessel beam arrays through dammann gratings," *Applied Optics*, vol. 51, no. 9, pp. 1375–1381, 2012.

[51] S. Kang and K. Oh, "1d bessel-like beam generation by highly directive transmission through a sub-wavelength slit embedded in periodic metallic grooves," *Optics Communications*, vol. 284, no. 22, pp. 5388–5393, 2011.

[52] X. Li, M. Pu, Z. Zhao, X. Ma, J. Jin, Y. Wang, P. Gao, and X. Luo, "Catenary nanostructures as compact bessel beam generators," *Scientific reports*, vol. 6, p. 20524, 2016.

[53] W.-T. Chen, M. Khorasaninejad, A. Y. Zhu, J. Oh, R. Devlin, A. Zaidi, and F. Capasso, "Generation of wavelength-independent and sub-wavelength bessel beams by meta-axicons," in *Frontiers in Optics*, p. FTh5B.6, Optical Society of America, 2016.

[54] E. Timurdogan, C. M. Sorace-Agaskar, J. Sun, E. S. Hosseini, A. Biberman, and M. R. Watts, "An ultralow power athermal silicon modulator," *Nature communications*, vol. 5, 2014.

[55] N. Li, P. Purnawirman, Z. Su, E. S. Magden, P. T. Callahan, K. Shtyrkova, M. Xin, A. Ruocco, C. Baiocco, E. P. Ippen, F. X. Kärtner, J. D. B. Bradley, D. Vermeulen, and M. R. Watts, "High-power thulium lasers on a silicon photonics platform," *Optics Letters*, vol. 42, no. 6, pp. 1181–1184, 2017.

[56] M. J. Byrd, E. Timurdogan, Z. Su, C. V. Poulton, N. M. Fahrenkopf, G. Leake, D. D. Coolbaugh, and M. R. Watts, "Mode-evolution-based coupler for high saturation power ge-on-si photodetectors," *Optics Letters*, vol. 42, no. 4, pp. 851–854, 2017.

[57] J. D. Bradley and E. S. Hosseini, "Monolithic erbium-and ytterbium-doped microring lasers on silicon chips," *Optics express*, vol. 22, no. 10, pp. 12226–12237, 2014.

[58] Z. Su, E. Timurdogan, D. Coleman, N. Fahrenkopf, T. Adam, G. Leake, D. Coolbaugh, D. Caplan, and M. R. Watts, "Second-order wavelength-selective partial-drop multicast filter bank," in *Integrated Photonics Research, Silicon and Nanophotonics*, pp. ITu1B–7, Optical Society of America, 2016.

[59] E. Timurdogan, Z. Su, K. Settaluri, S. Lin, S. Moazeni, C. Sun, G. Leake, D. D. Coolbaugh, B. Moss, M. Moresco, V. Stojanovič, and M. R. Watts, "An ultra low power 3d integrated intra-chip silicon electronic-photonic link," in *Optical Fiber Communication Conference*, pp. Th5B–8, Optical Society of America, 2015.

[60] V. R. Almeida, R. R. Panepucci, and M. Lipson, "Nanotaper for compact mode conversion," *Optics letters*, vol. 28, no. 15, pp. 1302–1304, 2003.

[61] J. Notaros, F. Pavanello, M. T. Wade, C. Gentry, A. Atabaki, L. Alloatti, R. J. Ram, and M. Popovic, "Ultra-efficient cmos fiber-to-chip grating couplers," in *Optical Fiber Communication Conference*, p. M2I.5, Optical Society of America, 2016.

[62] J. Notaros and M. Popović, "Band-structure approach to synthesis of grating couplers with ultra-high coupling efficiency and directivity," in *Optical Fiber Communication Conference*, pp. Th3F–2, Optical Society of America, 2015.

[63] J. Notaros and M. A. Popović, "Finite-difference complex-wavevector band structure solver for analysis and design of periodic radiative microphotonic structures," *Optics letters*, vol. 40, no. 6, pp. 1053–1056, 2015.

[64] L. B. Soldano and E. C. Pennings, "Optical multi-mode interference devices based on self-imaging: principles and applications," *Journal of Lightwave Technology*, vol. 13, no. 4, pp. 615–627, 1995.

[65] Y. Zhang, S. Yang, A. E.-J. Lim, G.-Q. Lo, C. Galland, T. Baehr-Jones, and M. Hochberg, "A compact and low loss y-junction for submicron silicon waveguide," *Optics express*, vol. 21, no. 1, pp. 1310–1316, 2013.

[66] M. Popović, *Theory and Design of High-Index-Contrast Microphotonic Circuits*. PhD thesis, Massachusetts Institute of Technology, 2008.

[67] M. R. Watts, J. Sun, C. DeRose, D. C. Trotter, R. W. Young, and G. N. Nielson, "Adiabatic thermo-optic mach–zehnder switch," *Optics letters*, vol. 38, no. 5, pp. 733–735, 2013.

[68] K. K. Mehta and R. J. Ram, "Precise and diffraction-limited waveguide-to-free-space focusing gratings," *arXiv preprint arXiv:1607.00107*, 2016.

[69] D. Taillaert, P. Bienstman, and R. Baets, "Compact efficient broadband grating coupler for silicon-on-insulator waveguides," *Optics letters*, vol. 29, no. 23, pp. 2749–2751, 2004.

[70] J. Sun, E. Timurdogan, A. Yaacobi, Z. Su, E. S. Hosseini, D. B. Cole, and M. R. Watts, "Large-scale silicon photonic circuits for optical phased arrays," *IEEE Journal of Selected Topics in Quantum Electronics*, vol. 20, no. 4, pp. 1–15, 2014.

[71] W. J. Westerveld, J. Pozo, S. M. Leinders, M. Yousefi, and H. P. Urbach, "Demonstration of large coupling-induced phase delay in silicon directional cross-couplers," *IEEE Journal of Selected Topics in Quantum Electronics*, vol. 20, no. 4, pp. 1–6, 2014.

[72] S. V. Deshpande, E. Gulari, S. W. Brown, and S. C. Rand, "Optical properties of silicon nitride films deposited by hot filament chemical vapor deposition," *Journal of Applied Physics*, vol. 77, no. 12, pp. 6534–6541, 1995.

[73] D. Tan, K. Ikeda, P. Sun, and Y. Fainman, "Group velocity dispersion and self phase modulation in silicon nitride waveguides," *Applied Physics Letters*, vol. 96, no. 6, p. 061101, 2010.

[74] D. Gu, W. Meiners, K. Wissenbach, and R. Poprawe, "Laser additive manufacturing of metallic components: materials, processes and mechanisms," *International materials reviews*, vol. 57, no. 3, pp. 133–164, 2012.